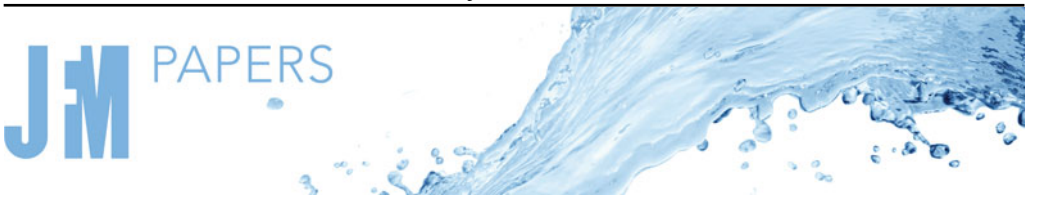
J. Fluid Mech. (2026), *vol.* 1038, A34, doi:10.1017/jfm.2026.11734



Pumping and steady streaming driven by two-frequency oscillations of a cylinder

Hyun S. Lee[1], **William D. Ristenpart**[2] **and Robert D. Guy**[1]

[1]Department of Mathematics, University California Davis, Davis, CA 95616, USA

[2]Department of Chemical Engineering, University of California Davis, Davis, CA 95616, USA

Corresponding author: Robert D. Guy, guy@math.ucdavis.edu

(Received 29 September 2025 UTC; revised 10 May 2026 UTC; accepted 16 May 2026 UTC)

The classical problem of steady streaming induced by an oscillating object has been studied extensively, but prior work has focused almost exclusively on single-frequency oscillations, which result in symmetric, quadrupole-like flows. Here we demonstrate that dual-frequency oscillations induce asymmetric steady streaming with a non-zero net flux in a direction determined by the polarity of the oscillation – the oscillator serves as a pump. We use numerical simulations and asymptotic analysis at small amplitude to examine two-dimensional steady streaming around a cylinder, first focusing on frequency ratio 2. The computational experiments show asymmetrical streaming and pumping, i.e. net flux downstream. It is well known from asymptotic analysis that steady streaming is second order in amplitude, and we show that pumping occurs at third order. We then extend the analysis to general frequency ratios, where we give necessary conditions for pumping, and predict the order in amplitude at which pumping occurs. Finally, we corroborate the theoretical results with computational simulations for different frequency ratios, and we discuss the implications for using dual-mode vibrations to pump fluids in lab-on-a-chip and other applications.

Key words: microfluidics, general fluid mechanics

1. Introduction

Steady streaming induced by an oscillating object is a classical phenomenon that has been studied analytically and experimentally (Riley 2001). The experimental study of steady streaming around a circular cylinder began with Carrière (1929) and Andrade (1931), who examined periodically oscillating air around a cylinder, and reported the now familiar quadrupole-like flow. Schlichting (1932) carried out the first asymptotic analysis of steady

© The Author(s), 2026. Published by Cambridge University Press. This is an Open Access article, distributed under the terms of the Creative Commons Attribution licence (https://creativecommons.org/licenses/by/4.0/), which permits unrestricted re-use, distribution and reproduction, provided the original article is properly cited.

https://doi.org/10.1017/jfm.2026.11734 Published online by Cambridge University Press

streaming around a cylinder, and he compared the solution with his experiments on a vibrating cylinder in water. In the small-amplitude limit, he matched the inner boundary layer with the outer potential flow, and his solution became the basis for future analysis. For example, Wang (1968) adapted the layer analysis to include the curvature of the boundary, which is relevant at higher order. Riley (1965) and Stuart (1966) analysed the problem at high Reynolds number where a second boundary layer exists, and their results agreed well with Schlichting's experiments. Finally, Holtsmark *et al.* (1954) analysed and solved the flow everywhere as a regular perturbation problem.

Though the problem of steady streaming has been studied extensively, past works have primarily focused on single-frequency oscillations, with comparatively less attention to multi-frequency oscillations (Davidson & Riley 1972; Kotas, Yoda & Rogers 2008). Davidson & Riley (1972) analysed steady streaming of multi-frequency oscillation around a cylinder, and found that the resultant flow is the superposition of steady streaming flows induced by each single-frequency oscillation. Similarly, Kotas *et al.* (2008) experimentally examined the steady flow around a sphere made to oscillate with two frequencies, and they found that the observed flows were the sum of the streaming flows from the respective single-frequency oscillations. The experiments in both of these works were carried out for small-amplitude motion in which the streaming velocity is small, and the asymptotic analysis was only performed up to second order in amplitude. There are reasons to believe that the imposition of multiple oscillatory frequencies might break the spatial symmetry and induce net flow in one direction at higher order in amplitude.

This work is inspired by recent experiments on a different physical system: an object sliding on a surface, undergoing two-frequency lateral oscillation (Hashemi *et al.* 2022). Specifically, the surface displacement was $(\ell/2)[\sin(\omega t) + \sin(\alpha\omega t)]$, where ℓ is the amplitude, ω is the frequency, and α is a ratio of the two frequencies. For particular α values, the object exhibited a net translation. To help to understand the experimental observations, they analysed a model in which the only force considered is the surface contact described by Coulomb's friction law. Representing the frequency ratio α as p/q, they derived a necessary condition for net motion – one of p or q is odd, and the other is even – and validated this prediction with experiments. For example, $\alpha = 2$, $3/2$ and $1/2$ showed net motion, while $\alpha = 1$, 3 and $5/3$ did not. We note that the same necessary conditions for directed motion were derived earlier by Reznik & Canny (2001) using a simpler friction model (Reznik, Canny & Goldberg 1997). Additional analysis and experiments for oscillations with different phase and amplitude were carried out in Zhang *et al.* (2024*a*), and Hui *et al.* (2024) further corroborated the theory with experiments with granular media.

In this work, we use computations and analysis to examine steady streaming around a cylinder, whose oscillation is the sum of two sinusoids of different frequencies. We show that a cylinder vibrating with two-frequency oscillation leads to pumping, i.e. a streaming flow with net directed motion of the surrounding fluid. We apply a small-amplitude analysis to study steady streaming for two-frequency oscillation at low Reynolds numbers. Indeed, at second order in amplitude, steady streaming is a superposition of streaming due to individual frequencies, consistent with prior observations; however, pumping is a higher-order effect and occurs only for certain frequency pairs. Obtaining expressions for higher-order terms is analytically intractable, but the form of the regular perturbation analysis allows us to deduce the structure of the solution and obtain necessary conditions for pumping.

The paper is organised as follows. In § 2, we introduce the motion of the cylinder and the non-dimensionalisation of the fluid equations. In § 3, we present numerical simulations for frequency ratio 2, and compare the flows with those of the single-frequency case.

https://doi.org/10.1017/jfm.2026.11734 Published online by Cambridge University Press

We measure the flux for varying amplitude, and we observe that pumping is a third-order effect. In § 4, we examine the asymptotic analysis of the problem at low amplitude. Even though we cannot solve the equations at third order, we show that a steady solution exists at third order and involves a net force responsible for pumping. Then, in § 5, we expand the analysis to general frequency ratios, and give necessary conditions for pumping, and we predict the order in amplitude at which pumping occurs. Finally, we confirm the theoretical results with computational simulations for select frequency ratios.

2. Problem statement

2.1. *Cylinder motion*

We use two related formulations of the problem: one in which the cylinder moves, and the other in which the cylinder is stationary and the far-field flow oscillates. For the moving cylinder formulation, a cylinder of radius R and centre $(X(t), 0)$ moves in a two-dimensional viscous fluid. The horizontal position of the cylinder's centre is prescribed as

$$X(t) = \frac{A}{2}[\sin(\Omega t) + \sin(\alpha \Omega t)], \tag{2.1}$$

where A is the amplitude of oscillation, Ω is the angular frequency of the base oscillation, and $\alpha \geq 1$, the ratio of the two frequencies. The frequency ratio is assumed rational so that the flow is time-periodic, and if we choose $\alpha = 1$, then we obtain the single-frequency case.

For analysis, it is convenient to consider the cylinder fixed at the origin, and impose a horizontal flow at infinity of strength

$$U(t) = -\frac{A\Omega}{2}[\cos(\Omega t) + \alpha \cos(\alpha \Omega t)]. \tag{2.2}$$

Furthermore, no-slip and no-penetration will be imposed, and the boundary conditions in two-dimensional cylindrical coordinates are

$$u_r(r = R) = 0, \quad u_\theta(r = R) = 0. \tag{2.3}$$

The two formulations are related by a change in reference frame. Switching our frame of reference from the inertial frame where the cylinder is oscillating to the non-inertial frame in which the cylinder is fixed results in a fictitious body force (Batchelor 2000)

$$F = -\rho\, U'(t)\, \boldsymbol{e}_x, \tag{2.4}$$

where ρ is the mass density, and $\boldsymbol{e}_x$ is the direction vector in the horizontal direction. In the non-inertial frame, we incorporate the fictitious body force (2.4) in the modified pressure defined as

$$\tilde{p} = p + \rho x\, U'(t). \tag{2.5}$$

For simplicity, we denote the modified pressure as p below.

2.2. *Non-dimensionalisation*

The equations are non-dimensionalised using characteristic length scale R, time scale Ω^{-1}, and velocity scale $R\Omega$. The flow around the cylinder is governed by the incompressible Navier Stokes equations:

$$Re\,(\boldsymbol{u}_t + \boldsymbol{u} \cdot \nabla \boldsymbol{u}) = -\nabla p + \Delta \boldsymbol{u}, \tag{2.6}$$

$$\nabla \cdot \boldsymbol{u} = 0, \tag{2.7}$$

https://doi.org/10.1017/jfm.2026.11734 Published online by Cambridge University Press

where the Reynolds number is

$$Re = \frac{R^2 \Omega}{\nu}, \tag{2.8}$$

and ν is the kinematic viscosity. The boundary conditions (2.2) and (2.3) become

$$u_r(r=1) = 0, \quad u_\theta(r=1) = 0, \tag{2.9}$$

and the horizontal flow at infinity is

$$U(t) = -\frac{\epsilon}{2}\left[\cos(t) + \alpha\cos(\alpha t)\right], \tag{2.10}$$

where

$$\epsilon = \frac{A}{R} \tag{2.11}$$

is the dimensionless amplitude of oscillation.

The Reynolds number $Re = R^2\Omega/\nu$ is based on the length scale of the cylinder's radius, and corresponds to the boundary layer in which viscous forces remain relevant. The streaming Reynolds number Re_s is based on the length scale of the oscillation amplitude, and it characterises the Reynolds number associated with the streaming flow. The two Reynolds numbers are related by

$$Re_s = \frac{A^2\Omega}{\nu} = \epsilon^2 Re. \tag{2.12}$$

The flow structure depends on both Re and Re_s. We refer to figure 1 of Chong *et al.* (2013) (which is adapted from figure 1 of Wang 1968) to illustrate the different flow regimes and associated analyses. Briefly, for high Reynolds numbers, the flow exhibits a boundary layer (Schlichting 1932; Wang 1968), and at high streaming Reynolds numbers, the streaming flow itself develops a second boundary layer (Riley 1965; Stuart 1966). At low Reynolds number, the problem can be analysed as a regular perturbation (Holtsmark *et al.* 1954) – though as noted in Chong *et al.* (2013), the regular perturbation solution from Holtsmark *et al.* (1954) contains the solution from the matched asymptotic analysis of Schlichting (1932) and Wang (1968), and is thus appropriate provided that the streaming Reynolds number is small. In this paper, we focus on the low streaming Reynolds number regime ($Re_s \ll 1$) so that the problem can be analysed as a regular perturbation, which allows us to compute the structure of solutions beyond second order needed to understand pumping from two-frequency oscillations.

3. Computational studies of frequency ratio 2

We begin by examining the flow patterns of streaming for frequency ratio $\alpha = 2$ using numerical simulations. The numerical methods are described in Appendix C. We consider other frequency ratios in § 5, where we show that $\alpha = 2$ yields the strongest pumping, and the difference of the flow pattern from the single-frequency case is subtle for other frequency ratios.

3.1. *Comparing flow patterns*

We place the cylinder in a square 8×8 domain with periodic boundary conditions, and solve for the flow at $Re = 10$. We solve for 250 periods, which is sufficiently long to allow the initial transient to decay, and the resulting flows are visualised by the positions of passive marker particles from the previous 10 periods of time. As expected for the

https://doi.org/10.1017/jfm.2026.11734 Published online by Cambridge University Press

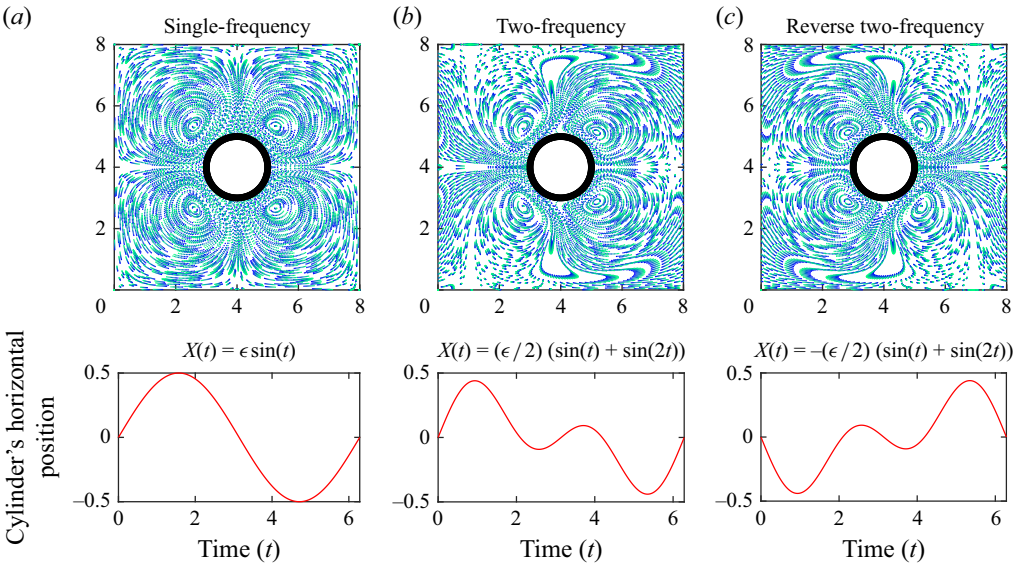


Figure 1. Streaming flows at time $T = 250$ for amplitude 0.5 and Reynolds number 10 for (*a*) single-frequency motion, (*b*) two-frequency motion, and (*c*) two-frequency motion with time reversal. Shown are the positions of passive tracer particles over 10 periods, where the current location is coloured green, and the location 10 periods prior is coloured blue. The domain is 8×8 with periodic boundary conditions. The bottom plots show the horizontal position of the cylinder's centre over one period.

single-frequency case in figure 1(*a*), the flow resembles the classical, four vortices associated with steady streaming. However, for two-frequency motion, shown in figures 1(*b*,*c*), the vortices are no longer symmetric and there is a net horizontal flow. The bottom plots show the cylinder's horizontal position for each case. In figure 1(*b*), the net flow is left to right – away from the cylinder, the green particles (most current period) are to the right of the blue particles (past period), indicating a net rightward flow. See supplementary movie 1 to compare the flow patterns of single-frequency, two-frequency and reverse two-frequency oscillations. We note that because of the periodic boundary conditions, these simulations correspond to a lattice of oscillating cylinders.

Figure 1(*c*) shows the flow resulting from the time-reversed, two-frequency motion of the cylinder. In this case, the flow is moving right to left, and the flow pattern appears to be the reflection about the vertical axis of the flow pattern from figure 1(*b*). The waveforms of the cylinders' positions for all three cases are depicted in the bottom row of figure 1. Note that the time-reversed waveform of the two-frequency oscillation is not a phase shift of the original, as in the single-frequency case. For the time-reversed oscillation, the flow is moving right to left, and the flow pattern appears to be the reflection about the vertical axis of the flow pattern from figure 1(*b*). This result demonstrates that the direction of the net flow is determined by the time asymmetry of the cylinder's motion. In the discussion, we elaborate on how the time symmetry of the cylinder motion for different frequency ratios is related to pumping. We note that a similar result was observed in the experiments of Hashemi *et al.* (2022) and Hui *et al.* (2024). When they reversed the polarity of the motion, the object translated in the opposite direction.

3.2. *Pumping in a channel*

The results in figure 1(*b*) suggest that cylinders oscillating with two frequencies can be used to pump fluids. To test that idea more directly, we repeated the computational

https://doi.org/10.1017/jfm.2026.11734 Published online by Cambridge University Press

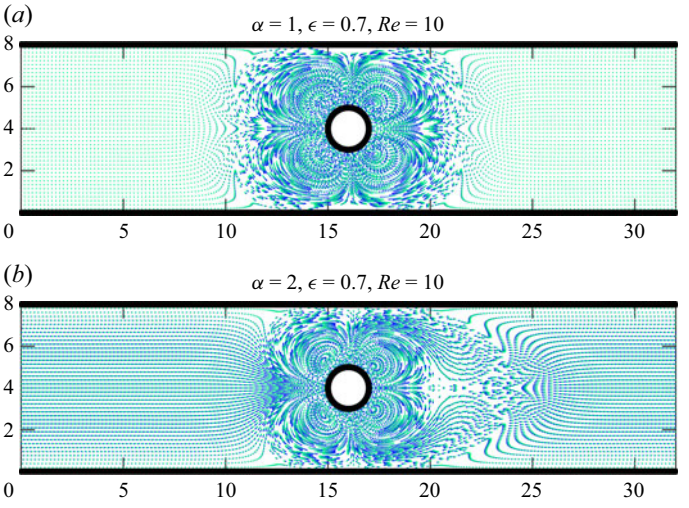


Figure 2. Streaming flows in a 32×8 channel for (a) single-frequency ($\alpha = 1$) and (b) two-frequency ($\alpha = 2$) oscillations at time $T = 250$ visualised with amplitude $\epsilon = 0.7$ and Reynolds number 10. Passive tracer particles highlight the positions of the flow from the last 10 periods. Shown are the positions of passive tracer particles over 10 periods, where the current location is coloured green, and the location 10 periods prior is coloured blue.

experiments in a channel of height 8 and length 32, with no-slip boundary conditions on the top and bottom, and periodic conditions in the horizontal direction. Figure 2 is a picture of supplementary movie 2 at time $T = 250$, showing the contrast of single- and two-frequency motions inside a channel. Again, for the single-frequency case, the four vortices align symmetrically around the cylinder, and particles away from the cylinder remain stationary. However, when the cylinder oscillates with two frequencies, the vortices lose their symmetry, and fluid is pumped to the right. Applying the negative waveform again reversed the direction of motion (results not shown).

Figure 3(a) shows the flux through a channel of height H,

$$Q(t) = \int_0^H u(x, y, t)\, \mathrm{d}y, \tag{3.1}$$

over 5 periods for both the single- and two-frequency cases for amplitude $\epsilon = 0.9$. The flux for the two-frequency case shows a non-zero average flux on the scale of approximately 10 % of the amplitude of the oscillation. We quantify pumping by the time average of the flux over the period T:

$$\langle Q(t) \rangle = \frac{1}{T} \int_{t-T}^{t} Q(\tau)\, \mathrm{d}\tau. \tag{3.2}$$

Figure 3(b) shows the period-averaged flux as a function of time for different amplitudes. For each amplitude, the period-averaged flux approaches a steady value that depends on the amplitude. The time-reversed oscillation results in the negative of the flux for the non-reversed oscillation of the same amplitude.

Figure 3(c) shows that the steady flux grows like amplitude cubed. For single-frequency oscillations, the magnitude of the steady flow is second order in amplitude, and the oscillatory component is first order (Holtsmark *et al.* 1954; Wang 1968; Chong *et al.* 2013). In figure 3(d), we show that for the two-frequency case, these same scalings for the sizes of the steady and oscillatory flows result as measured by the 2-norm of the period-averaged flow and the time average of the 2-norm of the velocity, respectively. Previously, analysis

https://doi.org/10.1017/jfm.2026.11734 Published online by Cambridge University Press

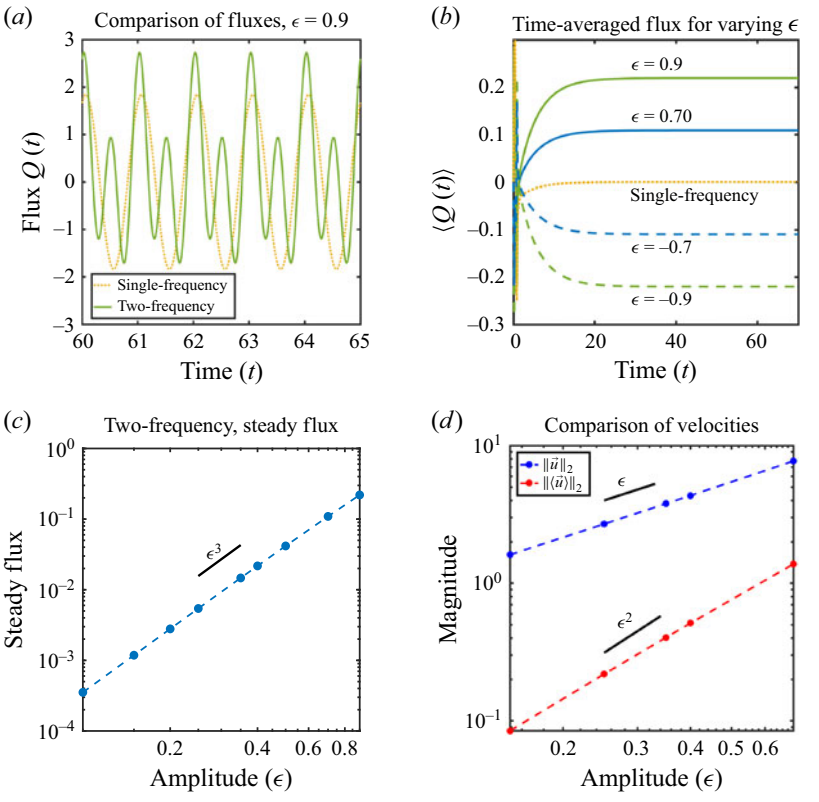


Figure 3. (*a*) Flux versus time is presented for both the single- and two-frequency cases for amplitude 0.9 and Reynolds number 10. (*b*) Time-averaged fluxes are shown for varying amplitudes ϵ. (*c*) The steady time-averaged flux is third order in amplitude for two-frequency oscillations. (*d*) The size of the oscillatory component, $\langle \|u\|_2 \rangle$, is first order in amplitude, and the size of the steady streaming flow, $\|\langle u \rangle\|_2$, is second order in amplitude for the two-frequency oscillation.

on steady streaming has only been carried out to second order in amplitude, so to derive the terms responsible for pumping, we need to extend the analysis to third order.

3.3. *Effect of Reynolds number on pumping*

We repeat the computational studies from the previous section at amplitude $\epsilon = 0.5$ and time $T = 300$ to examine how the flux and flow structure change with Reynolds number. We note that at $Re = 0$, the time-averaged flow is zero because of the dynamic reversibility of Stokes flow, and thus, there is no pumping at zero Reynolds number. Figure 4 shows the time-averaged flux for $10 \leq Re \leq 100$ at amplitude $\epsilon = 0.5$, frequency ratio $\alpha = 2$, and time $T = 300$. The flux grows with Reynolds number at a rate slightly larger than $\sqrt{Re}$.

In figure 5, we show the streamlines and normalised velocity vectors of the time-averaged flow for both single- and two-frequency cases at $Re = 10$ and $Re = 50$, which are above and below the critical Reynolds number (Chong *et al.* 2013) at which a boundary layer forms. At $Re = 10$ for the single-frequency case, we see the classical quadrupole-like structure, where the red streamlines indicate anticlockwise flow, and the blue streamlines indicate clockwise flow (figure 5*a*). For frequency ratio $\alpha = 2$, there is a clear flow to the right, and vortices are no longer left–right symmetric. At $Re = 50$, for both the single- and two-frequency cases, there is a region near the cylinder consisting of four rotating vortices with counter-rotating vortices outside this area (figures 5*c*,*d*). For two-frequency

https://doi.org/10.1017/jfm.2026.11734 Published online by Cambridge University Press

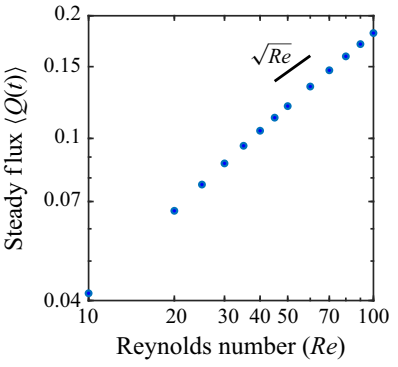


Figure 4. At amplitude $\epsilon = 0.5$, frequency ratio $\alpha = 2$, and time $T = 300$, the time-averaged fluxes for a 32×8 channel are measured for various Reynolds numbers. In general, the time-averaged fluxes appear to scale at a rate slightly larger than $\sqrt{Re}$.

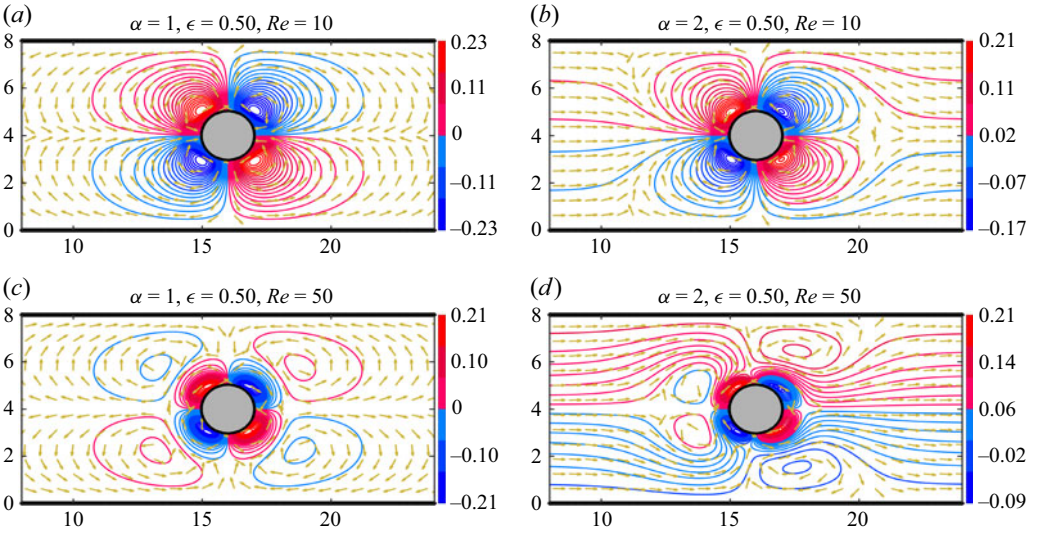


Figure 5. For a 32×8 channel at amplitude $\epsilon = 0.5$ and time $T = 300$, the streamlines and the flow directions (normalised velocity field) of the time-averaged flow are shown at frequency ratios (a,c) $\alpha = 1$ and (b,d) $\alpha = 2$, for (a,b) $Re = 10$ and (c,d) $Re = 50$.

oscillations, the net flow passes between the inner and outer vortices downstream from the cylinder. It should be noted that the near-cylinder region containing the inner vortices in figures 5(b,d) is sometimes referred to as the DC boundary layer to distinguish it from the thinner boundary layer associated with the oscillatory flow (Raney, Corelli & Westervelt 1954; Bertelsen, Svardal & Tjøtta 1973; Lutz, Chen & Schwartz 2005; Chong *et al.* 2013).

4. Low-amplitude analysis

We now analyse the problem in the limit of small amplitude ($\epsilon \ll 1$), and we restrict our analysis to small streaming Reynolds numbers ($Re_s \ll 1$) to apply a regular perturbation. The single-frequency solution has been previously computed through second order in amplitude (Holtsmark *et al.* 1954; Chong *et al.* 2013), but extending the analysis to third order is not analytically tractable. However, we derive the structure of the higher-order

https://doi.org/10.1017/jfm.2026.11734 Published online by Cambridge University Press

solutions, and from the structure alone, we can understand why pumping is a third-order effect for the two-frequency case.

4.1. *Governing equations*

We analyse the problem in terms of the stream function ψ, which is related to the velocity by

$$u_r = \frac{1}{r}\frac{\partial \psi}{\partial \theta}, \quad u_\theta = -\frac{\partial \psi}{\partial r}, \tag{4.1}$$

and

$$\boldsymbol{\nabla} \times \boldsymbol{u} = -\Delta\psi. \tag{4.2}$$

We take the curl of the momentum (2.6) to obtain

$$\left(\Delta - Re\frac{\partial}{\partial t}\right)\Delta\psi = Re\,\boldsymbol{u}\cdot\boldsymbol{\nabla}\,(\Delta\psi). \tag{4.3}$$

We solve the problem in the reference frame in which the cylinder is stationary with an oscillatory flow at infinity. The boundary conditions in terms of the stream function are

$$\psi(r=1) = 0, \quad \frac{\partial \psi}{\partial r}(r=1) = 0, \tag{4.4}$$

$$\psi \sim -\frac{\epsilon r}{2}\left(\cos(t) + 2\cos(2t)\right)\sin(\theta), \quad r \to \infty. \tag{4.5}$$

We consider the low-amplitude limit, and expand the solution in terms of $\epsilon = A/R$:

$$\psi = \epsilon\psi_1 + \epsilon^2\psi_2 + \epsilon^3\psi_3 + O\left(\epsilon^4\right). \tag{4.6}$$

Substituting the expansion into (4.3), (4.4) and (4.5), we obtain the successive equations at each order:

First Order

$$\left(\Delta - Re\frac{\partial}{\partial t}\right)\Delta\psi_1 = 0, \tag{4.7}$$

$$\psi_1(r=1) = 0, \quad \frac{\partial \psi_1}{\partial r}(r=1) = 0, \tag{4.8}$$

$$\psi_1 \sim -\frac{r}{2}\left(\cos(t) + 2\cos(2t)\right)\sin(\theta), \quad r \to \infty. \tag{4.9}$$

Second Order

$$\left(\Delta - Re\frac{\partial}{\partial t}\right)\Delta\psi_2 = Re\,\boldsymbol{u_1}\cdot\boldsymbol{\nabla}\,(\Delta\psi_1), \tag{4.10}$$

$$\psi_2(r=1) = 0, \quad \frac{\partial \psi_2}{\partial r}(r=1) = 0, \tag{4.11}$$

$$\psi_2 \sim 0, \quad r \to \infty. \tag{4.12}$$

Third Order

$$\left(\Delta - Re\frac{\partial}{\partial t}\right)\Delta\psi_3 = Re\,\boldsymbol{u_1}\cdot\boldsymbol{\nabla}\,(\Delta\psi_2) + Re\,\boldsymbol{u_2}\cdot\boldsymbol{\nabla}\,(\Delta\psi_1), \tag{4.13}$$

$$\psi_3(r=1) = 0, \quad \frac{\partial \psi_3}{\partial r}(r=1) = 0, \tag{4.14}$$

$$\psi_3 \sim 0, \quad r \to \infty. \tag{4.15}$$

https://doi.org/10.1017/jfm.2026.11734 Published online by Cambridge University Press

4.2. *Solution structure*

4.2.1. *Single-frequency oscillation*

Before we consider the two-frequency case, we first examine the solution structure for single-frequency oscillation. The only difference in the equations for the single-frequency and two-frequency cases is the boundary condition at infinity at first order. For the single-frequency case, (4.9) is replaced by

$$\psi_1 \sim -r\cos(t)\sin(\theta). \tag{4.16}$$

This boundary condition determines the form of the solution at first order as

$$\psi_1 = \mathrm{Re}\big(a_1(r)\,\mathrm{e}^{-\mathrm{i}t}\big)\sin(\theta), \tag{4.17}$$

where $\mathrm{Re}(z)$ denotes the real part of z. Analytically, $a_1(r)$ is a solution composed of Hankel functions (Watson 1922). We substitute (4.17) into the quadratic nonlinearity on the right-hand side of (4.10) to determine the form of the solution at second order. This computation involves all products of $\mathrm{e}^{-\mathrm{i}t}$ and $\mathrm{e}^{\mathrm{i}t}$, which results in a steady term and terms proportional to $\mathrm{e}^{\pm\mathrm{i}2t}$. Therefore, at second order, we obtain

$$\psi_2 = \mathrm{Re}\big(b_2(r)\,\mathrm{e}^{-2\mathrm{i}t}\big)\sin(2\theta) + b_0(r)\sin(2\theta). \tag{4.18}$$

Equation (4.13) at third order involves products of (4.17) and (4.18) on its right-hand side. This computation involves products of $\mathrm{e}^{\pm\mathrm{i}t}$ with 1 and with $\mathrm{e}^{\pm2\mathrm{i}t}$, which results in terms proportional to $\mathrm{e}^{\pm\mathrm{i}3t}$ and $\mathrm{e}^{\pm\mathrm{i}t}$. The third-order solution is of the form

$$\psi_3 = \mathrm{Re}\big(c_3(r)\,\mathrm{e}^{-\mathrm{i}3t} + c_1(r)\,\mathrm{e}^{-\mathrm{i}t}\big)\sin(3\theta) + \mathrm{Re}\big(d_3(r)\,\mathrm{e}^{-\mathrm{i}3t} + d_1(r)\,\mathrm{e}^{-\mathrm{i}t}\big)\sin(\theta). \tag{4.19}$$

Therefore, for the single-frequency case, there is no steady term at third order.

4.2.2. *Two-frequency oscillation*

For the two-frequency case, we obtain

$$\psi_1 = \mathrm{Re}\big(a_1(r)\,\mathrm{e}^{-\mathrm{i}t} + a_2(r)\,\mathrm{e}^{-2\mathrm{i}t}\big)\sin(\theta) \tag{4.20}$$

as the solution to (4.7)–(4.9). As before, we substitute the solution at first order into the right-hand side of (4.10) to deduce the structure of the second-order solution as

$$\begin{aligned}\psi_2 &= \mathrm{Re}\left(\sum_{k=1}^{4} b_k(r)\,\mathrm{e}^{-\mathrm{i}kt}\right)\sin(2\theta) + b_0^{(1)}(r)\sin(2\theta) + b_0^{(2)}(r)\sin(2\theta)\\ &= \mathrm{Re}\Big(\big(b_2(r)\,\mathrm{e}^{-2\mathrm{i}t} + b_0^{(1)}(r)\big) + \big(b_4(r)\,\mathrm{e}^{-4\mathrm{i}t} + b_0^{(2)}(r)\big)\\ &\quad + \big(b_1(r)\,\mathrm{e}^{-\mathrm{i}t} + b_3(r)\,\mathrm{e}^{-3\mathrm{i}t}\big)\Big)\sin(2\theta).\end{aligned} \tag{4.21}$$

We express the solution in this second form with three pairs of terms grouped together to highlight the origins of the different terms in the sum. The first two pairs involving a steady term and unsteady term correspond to the single-frequency solutions from each of the two driving frequencies, and the last pair of unsteady terms arises from the interaction between the driving frequencies. Thus as has been reported previously, the steady flow at second order is the superposition of two streaming fields caused by the individual, single-frequency oscillations (Davidson & Riley 1972; Kotas *et al.* 2008).

The nonlinear interaction between the two frequencies only affects the unsteady terms at second order, but these interactions produce a steady flow at third order. The solution at

https://doi.org/10.1017/jfm.2026.11734 Published online by Cambridge University Press

third order has the form

$$\psi_3 = \mathrm{Re}\left(\sum_{k=1}^{6} c_k(r)\,\mathrm{e}^{-\mathrm{i}kt}\right)\sin(3\theta) + c_0(r)\sin(3\theta) + \mathrm{Re}\left(\sum_{k=1}^{6} d_k(r)\,\mathrm{e}^{-\mathrm{i}kt}\right)\sin(\theta) + d_0(r)\sin(\theta). \tag{4.22}$$

Unlike the single-frequency solution (4.19), there are steady terms at third order in amplitude. In the following subsections, we explain how the third-order, steady terms produce the observed left–right asymmetry and are responsible for producing a net force that pumps the fluid.

4.3. *Symmetry of steady flow*

To illustrate how the steady flows at third order create asymmetry, consider the steady solution

$$\psi^s = \epsilon^2\, b(r)\sin(2\theta) + \epsilon^3\, c(r)\sin(3\theta) + \epsilon^3\, d(r)\sin(\theta) + O\left(\epsilon^4\right). \tag{4.23}$$

We show that the familiar second-order flow has a spatial symmetry different from that of the third-order flow that arises from the interactions of the flows generated by the two different driving frequencies. Specifically, the spatial symmetry arises from the θ-dependence of the stream functions. To illustrate these symmetries, we examine the streamlines of the three stream functions

$$\psi_2 = f(r)\sin(2\theta), \quad \psi_3^{(1)} = f(r)\sin(\theta), \quad \psi_3^{(3)} = f(r)\sin(3\theta), \tag{4.24}$$

where

$$f(r) = \frac{(r-1)^2}{1+r^4}. \tag{4.25}$$

This choice of $f(r)$ satisfies the boundary conditions on the cylinder and decays to zero at infinity, but it is not related to the solution of the equations.

The streamlines of ψ_2, $\psi_3^{(1)}$, $\psi_3^{(3)}$ are shown in figures 6(*a–c*), while the streamlines of the weighted sum are presented in figure 6(*d*). All the terms share a common up–down symmetry where the values at the points reflected across the horizontal axis are opposite in sign. Specifically, the stream functions are odd in y, i.e.

$$\psi_2(x,-y) = -\psi_2(x,y), \quad \psi_3^{(1)}(x,-y) = -\psi_3^{(1)}(x,y), \quad \psi_3^{(3)}(x,-y) = -\psi_3^{(3)}(x,y), \tag{4.26}$$

and the sum of the stream functions maintains this up–down symmetry. However, ψ_2 has a different left–right symmetry from the symmetry shared by the ψ_3 terms. Specifically, ψ_2 is odd in x, while the ψ_3 terms are even in x:

$$\psi_2(-x,y) = -\psi_2(x,y), \quad \psi_3^{(1)}(-x,y) = \psi_3^{(1)}(x,y), \quad \psi_3^{(3)}(-x,y) = \psi_3^{(3)}(x,y). \tag{4.27}$$

Therefore, the sum of the stream functions, illustrated in figure 6(*d*), retains the up–down symmetry, but lacks the left–right symmetry.

4.4. *Net force*

We compute the net force on the cylinder, and show that the steady term proportional to $\sin(\theta)$ that appears at third order for two-frequency oscillations indicates that there is a net

https://doi.org/10.1017/jfm.2026.11734 Published online by Cambridge University Press

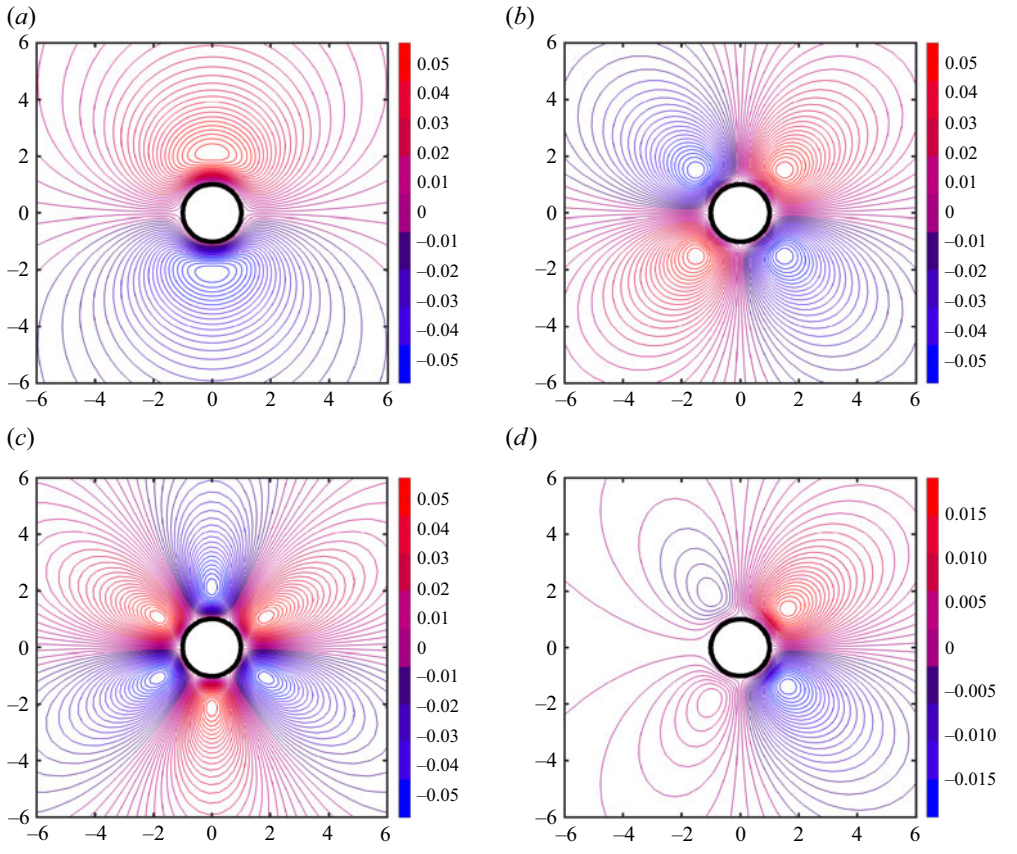


Figure 6. The contours of the stream functions are shown for (*a*) $\psi_2 = f(r)\sin(2\theta)$, (*b*) $\psi_3^{(1)} = f(r)\sin(\theta)$, and (*c*) $\psi_3^{(3)} = f(r)\sin(3\theta)$, where $f(r)$ is defined by (4.25). (*d*) Streamlines of the sum $\psi = \epsilon^2 f(r)\sin(2\theta) + \epsilon^3 f(r)\sin(3\theta) + \epsilon^3 f(r)\sin(\theta)$ for $\epsilon = 0.45$ exhibit a left–right asymmetry.

force on the cylinder. Assume a steady solution of the form

$$\psi^s = \sum_{k=1}^{\infty} f_k(r)\sin(k\theta). \tag{4.28}$$

The pressure can be computed using the momentum (2.6) to obtain

$$p^s = p_\infty + \sum_{k=1}^{\infty} g_k(r)\cos(k\theta). \tag{4.29}$$

The traction force in the horizontal direction is

$$\left(\sigma \cdot \hat{e}_r\right) \cdot \hat{e}_x = \sigma_{rr}\cos(\theta) - \sigma_{r\theta}\sin(\theta), \tag{4.30}$$

where $\hat{e}_r$ and $\hat{e}_x$ are the direction vectors for the r- and x-directions, respectively, and σ is the stress tensor. Using the boundary conditions on the cylinder from (2.9), the components of the stress on the cylinder are

$$\sigma_{rr} = -p_\infty - \sum_{k=1}^{\infty} g_k(1)\cos(k\theta), \quad \sigma_{r\theta} = -\sum_{k=1}^{\infty} f_k''(1)\sin(k\theta). \tag{4.31}$$

https://doi.org/10.1017/jfm.2026.11734 Published online by Cambridge University Press

Integrating the surface stress (4.30) over the cylinder, all the terms corresponding to $k \geq 2$ vanish due to symmetry, and the net horizontal force is

$$\text{net force} = \int_0^{2\pi} \left(\sigma_{rr}\cos(\theta) - \sigma_{r\theta}\sin(\theta)\right) \mathrm{d}\theta = \pi\left(-g_1(1) + f_1''(1)\right). \tag{4.32}$$

Therefore the term proportional to $\sin(\theta)$ that appears at third order in (4.23) contributes a net force that is responsible for the observed pumping.

This force calculation gives insight as to why pumping does not occur for the single-frequency case. From § 4.2.1, the only steady term through third order in amplitude is proportional to $\sin(2\theta)$, and the only non-zero term in the pressure expansion, (4.29), is proportional to $\cos(2\theta)$. Therefore there is no net force for single-frequency oscillations through third order in amplitude, though we have not yet considered the possibility of a net force resulting at higher order for the single-frequency case. In the next section, we analyse the form of the solution at higher orders, and we extend the analysis to general frequency ratio to derive necessary conditions on the frequency ratio for pumping.

5. Analysis of general frequency ratios

In the previous section, we showed that the steady stream function for frequency ratio $\alpha = 2$ contained a term at third order proportional to $\sin(\theta)$. In this section, we examine the solution structure of ψ_n, the solution to the nth-order perturbative equation (5.6), to determine whether there is potentially a net force on the fluid due to the presence of a $\sin(\theta)$ term in the expansion, and if so, what order.

For this analysis, it is convenient to express the motion of the cylinder as

$$X(t) = \frac{\epsilon}{2}\left(\sin(at) + \sin(bt)\right), \tag{5.1}$$

where $\gcd(a, b) = 1$. This expression is a slight modification from (2.1), and it amounts to a different definition of the Reynolds number from the one used in the previous sections. We again change reference frames by fixing the cylinder, and the governing equations have the form

$$\left(\Delta - Re\frac{\partial}{\partial t}\right)\Delta\psi = Re\,\boldsymbol{u}\cdot\nabla\left(\Delta\psi\right), \tag{5.2}$$

$$\psi(r=1) = 0, \quad \frac{\partial\psi}{\partial r}(r=1) = 0, \tag{5.3}$$

$$\psi \sim -\frac{\epsilon r}{2}\left(a\cos(at) + b\cos(bt)\right)\sin(\theta), \quad r \to \infty. \tag{5.4}$$

Expanding

$$\psi = \epsilon\psi_1 + \epsilon^2\psi_2 + \epsilon^3\psi_3 + O\left(\epsilon^4\right) \tag{5.5}$$

in the low-amplitude limit, and substituting this expansion into (5.2), we obtain successive equations of the form

$$\Delta\left(\Delta - Re\,\frac{\partial}{\partial t}\right)\psi_n = \sum_{i+j=n} Re\,\boldsymbol{u}_i\cdot\nabla(\Delta\psi_j). \tag{5.6}$$

The boundary conditions on the cylinder at each order are

$$\psi_n(r=1) = 0, \quad \frac{\partial\psi_n}{\partial r}(r=1) = 0, \tag{5.7}$$

https://doi.org/10.1017/jfm.2026.11734 Published online by Cambridge University Press

and the asymptotic condition at $r = \infty$ is

$$\psi_n \sim \begin{cases} \dfrac{-r}{2}\left(a\cos(at) + b\cos(bt)\right)\sin(\theta), & n = 1,\ r \to \infty, \\ 0, & n > 1,\ r \to \infty. \end{cases} \tag{5.8}$$

The solution to (5.6)–(5.8) is of the form

$$\psi_n = \sum_{m=1}^{\infty} \sum_{k,m=-\infty}^{\infty} f_{k,m}^{n}(r)\sin(m\theta)\,\mathrm{e}^{\mathrm{i}kt}, \tag{5.9}$$

but the number of non-zero terms is finite at each order. The boundary condition determines the non-zero terms at leading order, and at higher orders, the structure of the solution depends on the products of the lower-order terms. In the following subsections, we first determine which terms proportional to $\sin(m\theta)$ are non-zero at each order, then derive conditions for the presence of a steady term ($k = 0$).

5.1. *The θ-dependent terms*

From the form of the far-field boundary condition (5.8), the leading-order solution is of the form

$$\psi_1 = \mathrm{Re}\left(a_2(r)\,\mathrm{e}^{-\mathrm{i}bt} + a_1(r)\,\mathrm{e}^{-\mathrm{i}at}\right)\sin(\theta) = C_1(r,t)\sin(\theta). \tag{5.10}$$

The form of the right-hand side of (5.6) dictates the solution structure at higher orders. Substituting ψ_1 into the quadratic nonlinearity, the right-hand side of (5.6) is proportional to $\sin(\theta)\cos(\theta)$, thus the solution is proportional to $\sin(2\theta)$. Therefore, ψ_2 is of the form

$$\begin{aligned}\psi_2 &= \mathrm{Re}\left(b_4(r)\,\mathrm{e}^{-\mathrm{i}2bt} + b_3(r)\,\mathrm{e}^{-\mathrm{i}(a+b)t} + b_2(r)\,\mathrm{e}^{-\mathrm{i}2at} + b_1(r)\,\mathrm{e}^{-\mathrm{i}(a-b)t} + b_0(r)\right)\sin(2\theta) \\ &= C_2(r,t)\sin(2\theta).\end{aligned} \tag{5.11}$$

The right-hand side of (5.6) for ψ_3 involves the products of derivatives of ψ_1 and ψ_2. We obtain terms involving $\sin(2\theta)\cos(\theta)$ and $\sin(\theta)\cos(2\theta)$. Using the trigonometric identities

$$2\sin(2\theta)\cos(\theta) = \sin(3\theta) + \sin(\theta), \quad 2\sin(\theta)\cos(2\theta) = \sin(3\theta) - \sin(\theta), \tag{5.12}$$

ψ_3 can be expressed as

$$\psi_3 = C_3(r,t)\sin(3\theta) + C_4(r,t)\sin(\theta). \tag{5.13}$$

Similarly, the solution for ψ_4 has the form

$$\psi_4 = C_5(r,t)\sin(4\theta) + C_6(r,t)\sin(2\theta). \tag{5.14}$$

The first four orders show that the solution for odd values of n involves terms proportional to $\sin(m\theta)$ for odd values of m to $n = m$, and similarly for even values of n. In Appendix A, we prove a lemma that shows that this pattern holds for all n for a general multi-modal oscillation. Additionally, we prove an analogous result for the pressure. From § 4.4, a net horizontal force requires a term in the steady stream function proportional to $\sin(\theta)$, or a term in the steady pressure proportional to $\cos(\theta)$. Putting these two results together leads to the following necessary condition for pumping.

RESULT 5.1. *A necessary condition for pumping is the existence of an odd-valued n such that ψ_n has a steady component.*

https://doi.org/10.1017/jfm.2026.11734 Published online by Cambridge University Press

In the next subsection, we examine the frequencies that occur at each order, and derive conditions for pumping based on the frequency ratio.

5.2. *Necessary conditions for pumping*

5.2.1. *No pumping for single frequency*

We demonstrate that single-frequency oscillations do not pump by showing that ψ_n cannot have a steady component when n is odd. We examine the frequencies that arise at each order, and deduce the orders at which the steady terms occur. For example, figure 5 of Willis & Hohenegger (2024) illustrates how the frequencies at each order arise from the lower-order frequencies for the single-frequency case.

The structure of the leading-order solution for the single-frequency case ($a = b = 1$) is given in (4.17). Alternatively, we can express the solution as

$$\psi_1 = G_1^1(r,\theta)\,\mathrm{e}^{-\mathrm{i}t} + \overline{G_1^1(r,\theta)}\,\mathrm{e}^{\mathrm{i}t}, \tag{5.15}$$

where

$$G_1^1(r,\theta) = \frac{a_1(r)\sin(\theta)}{2}. \tag{5.16}$$

Similarly, the second-order solution (4.18) is rewritten as

$$\psi_2 = G_2^2(r,\theta)\,\mathrm{e}^{-\mathrm{i}2t} + \overline{G_2^2(r,\theta)}\,\mathrm{e}^{\mathrm{i}2t} + G_0^2(r,\theta), \tag{5.17}$$

where

$$G_2^2(r,\theta) = \frac{b_2(r)\sin(2\theta)}{2}, \quad G_0^2(r,\theta) = b_0(r)\sin(2\theta). \tag{5.18}$$

The time dependence of the individual terms in ψ_2, i.e. $\mathrm{e}^{-2\mathrm{i}t}$, $\mathrm{e}^{2\mathrm{i}t}$ and $1 = \mathrm{e}^{\mathrm{i}0t}$, result from the products of $\mathrm{e}^{-\mathrm{i}t}$ and $\mathrm{e}^{\mathrm{i}t}$ through the quadratic nonlinearity of the right-hand side of (5.6). Extending the pattern to higher-order n, if ψ_n has the term proportional to $\mathrm{e}^{\mathrm{i}\omega t}$, then

$$\mathrm{e}^{\mathrm{i}\omega t} = \left(\mathrm{e}^{-\mathrm{i}t}\right)^{n_1}\left(\mathrm{e}^{\mathrm{i}t}\right)^{n_2}, \tag{5.19}$$

where $n_1 + n_2 = n$ and $0 \le n_1, n_2 \le n$.

Now we show that the steady component cannot appear when n is odd. Using the fact that $n_2 = n - n_1$, we have

$$\omega = -n_1 + n_2 = -2n_1 + n. \tag{5.20}$$

For the steady term to appear ($\omega = 0$), n must be even. Combining this result with Result 5.1 shows that pumping does not occur for single-frequency oscillations.

5.2.2. *Two frequencies*

The two-frequency case involves products of $\mathrm{e}^{\pm\mathrm{i}at}$ and $\mathrm{e}^{\pm\mathrm{i}bt}$, leading to a more complicated analysis. However, using a similar parity argument, we obtain the following results.

RESULT 5.2. *Suppose that a and b are both odd, and ψ_n is the solution of (5.6)–(5.8). Steady terms appear only for n even, thus pumping will not occur.*

RESULT 5.3. *Suppose that only one of a or b is even (and the other is odd), and ψ_n is the solution of (5.6)–(5.8). Then ψ_n can have a steady component for n odd if $n \ge (a + b)$. Therefore the minimum order at which pumping occurs is order $a + b$.*

https://doi.org/10.1017/jfm.2026.11734 Published online by Cambridge University Press

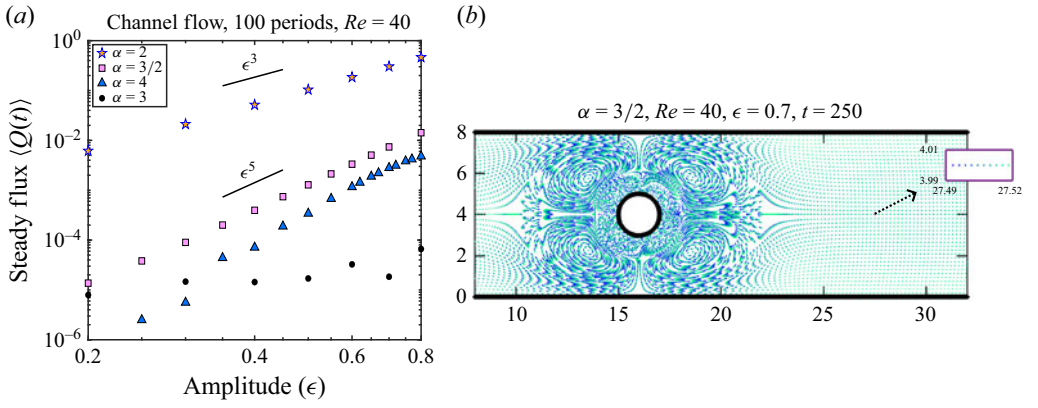


Figure 7. (*a*) Time-averaged flux versus amplitude for frequency ratios $\alpha = 2$, $3/2$, 4 and 3. (*b*) Steady streaming in a channel for frequency ratio $\alpha = 3/2$ visualised at amplitude 0.7 and Reynolds number 40. Shown are the positions of passive tracer particles over 10 periods where the current location is coloured green, and the location 10 periods prior is coloured blue. Though the fluid is being pumped, net motion is not obvious on this scale. The inset shows the region around a single tracer particle, which confirms that the fluid is moving slowly downstream.

See Appendix B for the proofs of Results 5.2 and 5.3. In Result 5.3, we give the smallest order of amplitude at which pumping can occur; however, we do not guarantee pumping. For simplicity, we defined the radial components as coefficients in the analysis, but these coefficients could equate to zero.

5.3. *Numerical results for other frequency ratios*

According to Result 5.3, for small amplitude ϵ, the strength of pumping scales like ϵ^n, where $n = a + b$ is the sum of the two frequencies and must be odd. Thus the strongest pumping results when $n = 3$, corresponding to frequency ratio $\alpha = 2$. The next smallest order at which pumping can occur is fifth order. From Result 5.3, a fifth-order scaling can occur only when the frequency ratio is $3/2$ or 4, respectively corresponding to $a = 2,\ b = 3$ or $a = 1,\ b = 4$. Figure 7(*a*) shows the fluxes from numerical simulations for different frequency ratios and amplitudes, and these results verify that pumping is fifth order in amplitude for frequency ratios $3/2$ and 4. Moreover, the fluxes for frequency ratios $3/2$ and 4 are significantly smaller than the fluxes for frequency ratio 2. For example, at amplitude 0.7, the flux of frequency ratio 2 is approximately 41 times larger than the flux at frequency ratio $3/2$. In figure 7(*b*), we show the passive tracer particles over 10 periods, and the net flow is not obvious without zooming in closely or playing supplementary movie 3. Though the fluxes for frequency ratios $3/2$ and 4 are small, they show clear scaling with amplitude. By contrast, the small fluxes for frequency ratio 3 are not correlated with the amplitude. According to Result 5.3, there is no pumping for frequency ratio 3, and the small fluxes reported in figure 7(*a*) arise from numerical error. Note that in § 3.2, we examined how the flux scaled with amplitude for $\alpha = 2$ at $Re = 10$. Here, we use $Re = 40$ because at lower Reynolds numbers, the fluxes are small, and it is difficult to measure pumping at higher order. We note that the analysis was performed in the limit of small amplitude, and is expected to be valid for small streaming Reynolds numbers. The fluxes reported in figure 7(*a*) were computed at streaming Reynolds numbers in the range 1.6–25.6, yet we obtained excellent agreement with the analysis.

https://doi.org/10.1017/jfm.2026.11734 Published online by Cambridge University Press

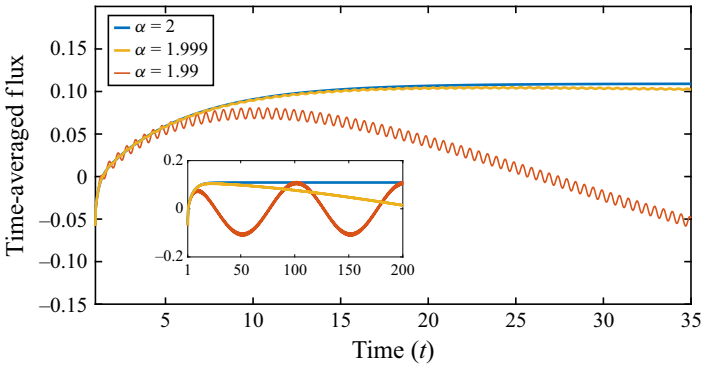


Figure 8. Time averages of fluxes over one time unit for frequency ratios $\alpha = 2$, 1.999 and 1.99 at amplitude $\epsilon = 0.7$ and $Re = 10$. The inset shows the time-averaged fluxes to time 200. On short time scales, the fluxes are similar, but on long time scales, the fluxes for $\alpha = 1.99$ and 1.999 oscillate with amplitude similar to the steady flux for $\alpha = 2$.

5.4. *Near-miss frequencies*

An interesting question is what happens for frequency ratios that are close to, but not equal to, $\alpha = 2$. Figure 8 shows the fluxes averaged over one time unit for frequency ratios $\alpha = 2$, 1.999 and 1.99 at amplitude $\epsilon = 0.7$ and $Re = 10$. The fluxes for $\alpha = 1.99$ and 1.999 oscillate on long time scales, with periods 100 and 1000, respectively, with amplitude similar to the steady flux for $\alpha = 2$. According to Result 5.3, for $\alpha = 1.99$ and 1.999, the lowest orders in amplitude pumping that could occur are 299 and 2999, respectively. Over long periods, we expect negligible net flux for these 'near-miss' frequency ratios, but on a short time scale they exhibit fluxes similar to $\alpha = 2$.

6. Discussion

Using asymptotic analysis and numerical simulations, we examined the flow around a cylinder moving with two-frequency collinear oscillations, and we derived necessary conditions for pumping. Strikingly, the necessary conditions on the frequency ratio for non-zero net motion are identical to those observed in the physical system of objects sliding via frictional forces on a laterally vibrating surface (Reznik & Canny 2001; Hashemi *et al.* 2022). Hashemi *et al.* (2022) identified the time asymmetry of the driving oscillation necessary for net motion. Specifically, the sliding object exhibited net motion only when the vibrations were non-anti-periodic. A 2π-periodic function $f(t)$ is anti-periodic if there exists $0 < \phi < 2\pi$ such that

$$f(t) = -f(t + \phi). \tag{6.1}$$

Conversely, $f(t)$ is non-anti-periodic if $f(t)$ does not satisfy (6.1) for any ϕ. Hashemi *et al.* (2022) showed that for frequency ratio $\alpha = b/a$, the two-frequency oscillation in (2.1) is anti-periodic if both a and b are odd. Otherwise, the motion is non-anti-periodic; i.e. one of a or b is odd, and the other is even. For example, for $\alpha = 1/1$ and $\alpha = 3/1$, the motion is anti-periodic (i.e. (6.1) is satisfied for $\phi = \pi$), and for $\alpha = 2/1$, the motion is non-anti-periodic.

To help to illustrate the significance of anti-periodicity, in figure 9 we plot the cylinder's horizontal position for $\alpha = 1/1$, $\alpha = 3/1$ and $\alpha = 2/1$, and highlight the paths between the maximum and minimum positions. For an anti-periodic oscillation (e.g. $\alpha = 1$ and

https://doi.org/10.1017/jfm.2026.11734 Published online by Cambridge University Press

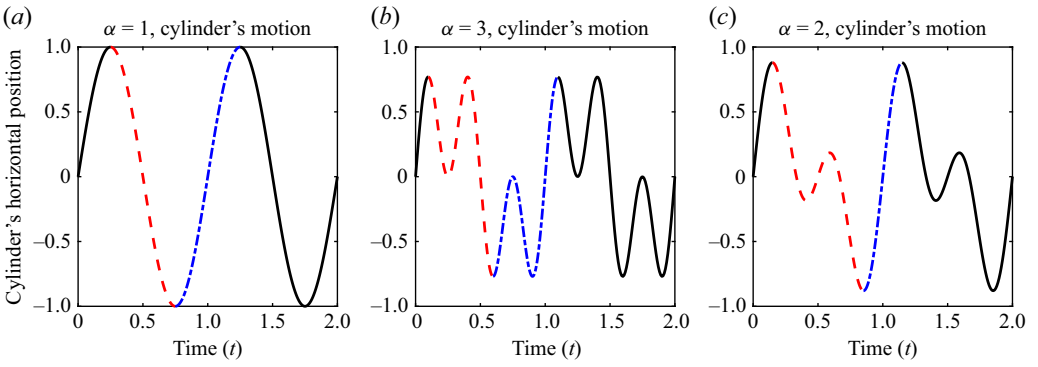


Figure 9. The displacement of the cylinder's centre, defined by (2.1), is plotted from $0 \leq t \leq 2$ for (*a*) $\alpha = 1$, (*b*) $\alpha = 3$, (*c*) $\alpha = 2$ when $A = 1$. The blue dash-dotted curve corresponds to the path from the leftmost to the rightmost position of the cylinder, and the red dashed curve shows the path from the rightmost to the leftmost position.

$\alpha = 3$), there is a symmetry between the path from the rightmost to the leftmost position (red dashed line) and the path from the leftmost to rightmost position (blue dash-dotted line). Based on this symmetry, one would not expect a net flow. For a non-anti-periodic oscillation (e.g. $\alpha = 2$), the cylinder's motion from the rightmost to leftmost position is distinct from its counterpart. In our simulations, we observed that this motion produced net flow to the right. One may suspect that the direction of the flow results from the larger average velocity along the path from its leftmost to rightmost positions compared to its opposite. This idea is consistent with the observed net flow to the left when $\alpha = -2$. The relationship between the waveform and the direction of flow is likely not so simple, and further analysis is required.

In this paper, we not only derived the necessary conditions for pumping, but also obtained the smallest order in amplitude at which pumping occurs. Frequency ratio 2 results in pumping at third order in amplitude, and all other frequency ratios produce pumping at higher order. This result indicates that pumping is strongest for frequency ratio 2 at small amplitude. In numerical simulations, we observed (figure 7*a*) that the flux for $\alpha = 2$ is at least 10 times larger than the flux from other frequency ratios. These results are consistent with those of Hashemi *et al.* (2022), who reported both experimentally and numerically that $\alpha = 2$ generated the largest net motion. Likewise, Reznik & Canny (2001) and Hui *et al.* (2024) showed in their models that the largest net frictional force was produced when the frequency ratio was $\alpha = 2$.

Some insight into the connection between the flow around an oscillating cylinder and the frictional sliding problem is provided by Hashemi, Gilman & Khair (2024), in which they analyse the movement of a particle in a tank of fluid undergoing two-frequency oscillations. The model involves linear and nonlinear drag forces induced by the relative motion of the particle and the surrounding fluid. They perform analysis in the small-amplitude limit, and show that only frequency ratio $\alpha = 2$ produces a non-zero time-averaged velocity at first order in amplitude. Like the streaming problem that we analyse, other frequency ratios produce net movement at higher order in amplitude. Hashemi *et al.* (2024) argues that models of both particles in an oscillating tank and an object sliding on a frictional surface are related to the same reduced model of a forced mechanical system with nonlinear dissipation.

https://doi.org/10.1017/jfm.2026.11734 Published online by Cambridge University Press

In our analysis and computational experiments, the two oscillations were of equal amplitude, in phase, and collinear. Analysis and experiments on sliding frictional systems have considered the more general motion of the form

$$X(t) = \frac{A_1}{2}\sin(\Omega_1 t) + \frac{A_2}{2}\sin(\Omega_2 t + \phi). \tag{6.2}$$

For example, it was predicted that for frequency ratio 2, the maximum sliding velocity occurs for $A_2/A_1 \approx 0.25$ (Reznik & Canny 1998; Zhang *et al.* 2024*a*), which was validated experimentally (Hui *et al.* 2024). The analysis from this work focused on necessary conditions on the frequency ratio for pumping based on the solution structure, and it does not predict how the pumping rate depends on parameters. The analytic solution can be obtained through second order (Holtsmark *et al.* 1954), but solving the resulting equations at third order and higher, where pumping occurs, is not feasible. The pumping rate for different amplitudes, phases and Reynolds numbers could be measured experimentally or numerically. We note that to our knowledge, there have been no experiments that examine the pumping rate generated by a cylinder oscillating with two frequencies. Another interesting generalisation of the motion involves non-collinear, two-frequency vibrations (i.e. oscillations with different frequencies in two different directions). It may be possible to extend the analysis of this work to derive necessary conditions for a temporal asymmetry, and hence a net-directed flow, but more work on this problem is needed.

Steady streaming has been exploited in many microfluidic applications, such as drug delivery (Sumner, Mestel & Reichenbach 2021), particle trapping (Wang *et al.* 2012*a*; Patel *et al.* 2014; Thameem, Rallabandi & Hilgenfeldt 2016; Agarwal, Rallabandi & Hilgenfeldt 2018; Mutlu, Edd & Toner 2018; Volk *et al.* 2020; Zhang *et al.* 2024*b*), bubble-driven flow (Marmottant *et al.* 2006; Wang, Rallabandi & Hilgenfeldt 2013; Rallabandi, Wang & Hilgenfeldt 2014), mixing (Liu, Lenigk & Grodzinski 2003; Ahmed *et al.* 2009; Kumar *et al.* 2011; Huang *et al.* 2013) and pumping (Marmottant & Hilgenfeldt 2004; Tovar & Lee 2009; Tovar, Patel & Lee 2011; Huang *et al.* 2014; Zhang & Rallabandi 2024). Microchannel pumps driven by single-frequency steady streaming rely on design asymmetry of the apparatus to produce a net-directed flow. For example, Tovar & Lee (2009) designed a micropump in which cavities of trapped air bubbles were placed at an angle along the channel walls. The angling of the cavities produces an asymmetric streaming flow that results in a net force that drives the flow through the channel. In our work, we have shown that a cylinder vibrating with two-frequency oscillations can pump fluid in either direction. The asymmetry in this case is temporal rather than spatial, and this idea could lead to new designs of microfluidic pumps, or potentially enhance the performance of existing designs.

The autonomous propulsion of microparticles is a means of transporting objects by steady streaming (Wang *et al.* 2012*b*; Nadal & Lauga 2014; Ahmed *et al.* 2016; Collis, Chakraborty & Sader 2017; Sabrina *et al.* 2018; Lippera *et al.* 2019; Nadal & Michelin 2020; Li *et al.* 2024). The particle or the background flow vibrates with single-frequency oscillations, and variation in particle shape or density leads to an asymmetric streaming flow that induces a net propulsive force on the particle. The asymptotic analysis of this phenomenon involves computing how the particle asymmetry leads to a net force on itself (Nadal & Lauga 2014; Collis *et al.* 2017). Our analysis illustrates how a net force can arise from temporal asymmetry through two-frequency oscillations of a symmetric object. Though our analysis was for a cylinder, it could be extended to a sphere. Based on our results, we predict that symmetric particles could be transported by employing two-frequency oscillations.

https://doi.org/10.1017/jfm.2026.11734 Published online by Cambridge University Press

Supplementary movies. Supplementary movies are available at https://doi.org/10.1017/jfm.2026.11734.

Funding. The work of W.D.R. was partially supported by the National Science Foundation under grant no. CBET2125806.

Declaration of interests. The authors report no conflict of interest.

Data availability statement. The source code for the numerical simulations is available from the corresponding author, R.D.G.

Appendix A. Spatial structure of the solution

We prove Result 5.1 in § 5 by proving a more general case involving multi-frequency oscillations. Suppose that the cylinder is oscillating in the horizontal direction:

$$X(t) = \epsilon \sum_{k=1}^{K} a_k \sin(kt + \phi_k). \tag{A1}$$

Then fixing the cylinder, the governing equations for multi-frequency oscillation are

$$\begin{gathered}\left(\Delta - Re\frac{\partial}{\partial t}\right)\Delta\psi = \epsilon\, Re\, \boldsymbol{u}\cdot\nabla\,(\Delta\psi),\\ \psi(r=1) = 0, \quad \frac{\partial\psi}{\partial r}(r=1) = 0,\\ \psi \sim \epsilon \sum_{k=-K}^{K} c_k r\, \mathrm{e}^{\mathrm{i}kt}\sin(\theta),\end{gathered} \tag{A2}$$

where

$$c_k = \frac{-\mathrm{sgn}(k)\, a_k k\, \mathrm{e}^{\mathrm{i}\,\mathrm{sgn}(k)\,\phi_k}}{2}, \quad c_0 = 0. \tag{A3}$$

Expanding in the small-amplitude limit,

$$\psi = \epsilon\psi_1 + \epsilon^2\psi_2 + \epsilon^3\psi_3 + O\left(\epsilon^4\right), \tag{A4}$$

the equations at the nth order are

$$\Delta\left(\Delta - Re\,\frac{\partial}{\partial t}\right)\psi_n = \sum_{i+j=n} Re\,\boldsymbol{u_i}\cdot\nabla(\Delta\psi_j), \tag{A5}$$

$$\psi_n(r=1) = 0, \quad \frac{\partial\psi_n}{\partial r}(r=1) = 0, \tag{A6}$$

$$\psi_n \sim \begin{cases} \displaystyle\sum_{k=-K}^{K}\left(c_k r\, \mathrm{e}^{\mathrm{i}kt}\right)\sin(\theta), & n = 1,\\ 0, & n > 1. \end{cases} \tag{A7}$$

From the stream function, the velocity is computed from (4.1), and the pressure can be found from substituting the velocity into the momentum (2.6).

To prove Result 5.1, we prove two lemmas in the following subsections that show that terms proportional to $\sin(\theta)$ and $\cos(\theta)$ only appear at odd order in the expansions for the velocity and pressure, respectively. In § 4.4, we showed that a net force requires such terms, which together with the lemmas proves Result 5.1.

https://doi.org/10.1017/jfm.2026.11734 Published online by Cambridge University Press

A.1. *Solution structure of ψ_n*

Equation (A5) has the general solution

$$\psi_n = \sum_{k,m=-\infty}^{\infty} f_{k,m}^n(r)\, \mathrm{e}^{\mathrm{i}kt}\, \mathrm{e}^{\mathrm{i}m\theta}, \tag{A8}$$

but the boundary conditions limit the solution to a finite number of terms. For example, the far-field boundary condition (A7) dictates the structure of ψ_1:

$$\psi_1 = \left(\sum_{k=-K}^{K} f_{k,1}^1(r)\, \mathrm{e}^{\mathrm{i}kt} \right) \sin(\theta) = F_1^1(r,t)\sin(\theta). \tag{A9}$$

Furthermore, the solution for ψ_2 is dependent on the quadratic nonlinearity of ψ_1 with itself, resulting in

$$\psi_2 = \left(\sum_{k=-2K}^{2K} f_{k,2}^2(r)\, \mathrm{e}^{\mathrm{i}kt} \right) \sin(2\theta) = F_2^2(r,t)\sin(2\theta). \tag{A10}$$

Generally, the interaction of lower-order terms determines the structure of ψ_n, and the following lemma shows that the solution structure depends on the parity of n.

LEMMA A.1. *For $n \in \mathbb{N}$, the solution of (A5) with its boundary conditions (A6) and (A7) has the form*

$$\psi_n \sim \begin{cases} \displaystyle\sum_{l=1}^{n/2} F_{2l}^n(r,t)\sin(2l\theta) & \textit{for } n \textit{ even}, \\ \displaystyle\sum_{l=0}^{(n-1)/2} F_{2l+1}^n(r,t)\sin\left((2l+1)\theta\right) & \textit{for } n \textit{ odd}. \end{cases} \tag{A11}$$

Proof. We will proceed with induction, and choose $n = 1$ and $n = 2$ as the base cases. From the boundary conditions (A6) and (A7),

$$\psi_1 = F_1^1(r,t)\sin(\theta). \tag{A12}$$

To solve for ψ_2, we compute the right-hand side of (A5):

$$Re\, \boldsymbol{u}_1 \cdot \nabla\left(\Delta\psi_1\right) = \frac{Re}{2}\left(\frac{1}{r} F_1^1(r,t) \cdot \frac{\partial}{\partial r} D_1 F_1^1(r,t) - \frac{1}{r}\frac{\partial}{\partial r} F_1^1(r,t) \cdot D_1 F_1^1(r,t) \right) \sin(2\theta), \tag{A13}$$

where

$$D_1 = \frac{\partial^2}{\partial r^2} + \frac{1}{r}\frac{\partial}{\partial r} - \frac{1}{r^2}. \tag{A14}$$

Therefore,

$$\psi_2 = F_2^2(r,t)\sin(2\theta). \tag{A15}$$

By induction, we assume that (A11) holds true up to ψ_{n-1}, and for simplicity, assume that n is odd. Proving the even case involves the same procedure. Note that each term of the right-hand side of (A5) consists of

$$\boldsymbol{u}_i \cdot \nabla\left(\Delta\psi_j\right) = \frac{1}{r}\frac{\partial\psi_i}{\partial\theta}\frac{\partial}{\partial r}\left(\Delta\psi_j\right) - \frac{1}{r}\frac{\partial\psi_i}{\partial r}\frac{\partial}{\partial\theta}\left(\Delta\psi_j\right), \tag{A16}$$

https://doi.org/10.1017/jfm.2026.11734 Published online by Cambridge University Press

where $i + j = n$. If we show that (A16) is a linear combination of $\{\sin(\theta), \sin(3\theta), \ldots, \sin(n\theta)\}$, then we have completed the induction.

Because n is odd, one of i and j is even, and the other is odd. Without loss of generality, choose i even and j odd. Substituting ψ_i and ψ_j into (A16), we obtain

$$\begin{aligned}\boldsymbol{u}_i \cdot \nabla\left(\Delta\psi_j\right) = &\sum_{s=1}^{i/2}\sum_{q=0}^{(j-1)/2} \frac{2s}{r} F^i_{2s}(r,t)\frac{\partial}{\partial r} D_{2q+1} F^j_{2q+1}(r,t)\sin((2q+1)\theta)\cos(2s\theta) \\ &-\sum_{s=1}^{i/2}\sum_{q=0}^{(j-1)/2} \frac{2q+1}{r} D_{2q+1} F^j_{2q+1}(r,t)\frac{\partial}{\partial r} F^i_{2s}(r,t)\sin(2s\theta)\cos((2q+1)\theta),\end{aligned} \tag{A17}$$

where

$$D_m = \frac{\partial^2}{\partial r^2} + \frac{1}{r}\frac{\partial}{\partial r} - \frac{m^2}{r^2}. \tag{A18}$$

We use the identity

$$2\sin(a\theta)\cos(b\theta) = \sin((a+b)\theta) + \sin((a-b)\theta), \quad a, b \in \mathbb{N}, \tag{A19}$$

to simplify (A17) to

$$\boldsymbol{u}_i \cdot \nabla\left(\Delta\psi_j\right) = \sum_{s=1}^{i/2}\sum_{q=0}^{(j-1)/2} A^{i,j^-}_{s,q}(r,t)\sin((2q+2s+1)\theta) + A^{i,j^+}_{s,q}(r,t)\sin((2q-2s+1)\theta), \tag{A20}$$

where

$$A^{i,j^\pm}_{s,q}(r,t) = \frac{s}{r}F^i_{2s}(r,t)\frac{\partial}{\partial r}D_{2q+1}F^j_{2q+1}(r,t) \pm \frac{2q+1}{2r}D_{2q+1}F^j_{2q+1}(r,t)\frac{\partial}{\partial r}F^i_{2s}(r,t). \tag{A21}$$

For $1 \le s \le i/2$ and $0 \le q \le (j-1)/2$,

$$3 \le |2q+2s+1| \le i + j = n, \quad 1 \le |2q-2s+1| \le \max\{|i-3|, |j-2|\}. \tag{A22}$$

In particular,

$$1 \le |2q+2s+1|,\ |2q-2s+1| \le n. \tag{A23}$$

Therefore, for some coefficients $F^n_{2l+1}(r,t)$,

$$\boldsymbol{u}_i \cdot \nabla\left(\Delta\psi_j\right) = \sum_{l=0}^{(n-1)/2} F^n_{2l+1}(r,t)\sin((2l+1)\theta), \tag{A24}$$

which completes the induction. □

A.2. *Solution structure of p_n*

To compute the pressure, we convert the stream function $\psi = \epsilon\psi_1 + \epsilon^2\psi_2 + \epsilon^3\psi_3 + \cdots$ into velocity components:

$$u_r = \epsilon u_{r,1} + \epsilon^2 u_{r,2} + \epsilon^3 u_{r,3} + O\left(\epsilon^4\right), \tag{A25a}$$

$$u_\theta = \epsilon u_{\theta,1} + \epsilon^2 u_{\theta,2} + \epsilon^3 u_{\theta,3} + O\left(\epsilon^4\right), \tag{A25b}$$

https://doi.org/10.1017/jfm.2026.11734 Published online by Cambridge University Press

where

$$u_{r,i} = \frac{1}{r}\frac{\partial \psi_i}{\partial \theta}, \quad u_{\theta,i} = -\frac{\partial \psi_i}{\partial r}. \tag{A26}$$

We expand the pressure in the small-amplitude limit,

$$p = \epsilon p_1 + \epsilon^2 p_2 + \epsilon^3 p_3 + O(\epsilon^4), \tag{A27}$$

and substitute the velocity components (A25) and the pressure (A27) into the momentum (2.6) to obtain successive equations at each order n:

$$\begin{aligned}\frac{\partial p_n}{\partial r} &= \Delta u_{r,n} - \frac{u_{r,n}}{r^2} - \frac{2}{r^2}\frac{\partial u_{\theta,n}}{\partial \theta} \\ &\quad - Re\frac{\partial u_{r,n}}{\partial t} - Re\sum_{i+j=n}\left(u_{r,i}\frac{\partial u_{r,j}}{\partial r} + \frac{u_{\theta,i}}{r}\frac{\partial u_{r,j}}{\partial \theta} - \frac{u_{\theta,i}u_{\theta,j}}{r}\right),\end{aligned} \tag{A28a}$$

$$\begin{aligned}\frac{1}{r}\frac{\partial p_n}{\partial \theta} &= \Delta u_{\theta,n} - \frac{u_{\theta,n}}{r^2} + \frac{2}{r^2}\frac{\partial u_{r,n}}{\partial \theta} \\ &\quad - Re\frac{\partial u_{\theta,n}}{\partial t} - Re\sum_{i+j=n}\left(u_{r,i}\frac{\partial u_{\theta,j}}{\partial r} + \frac{u_{\theta,i}}{r}\frac{\partial u_{\theta,j}}{\partial \theta} + \frac{u_{r,i}u_{\theta,j}}{r}\right).\end{aligned} \tag{A28b}$$

For future computations, it is convenient to work with the linear and nonlinear terms separately, so that

$$\frac{\partial p_n}{\partial r} = L_{r,n} + Re\sum_{i+j=n} NL_{r,i,j}, \tag{A29a}$$

$$\frac{1}{r}\frac{\partial p_n}{\partial \theta} = L_{\theta,n} + Re\sum_{i+j=n} NL_{\theta,i,j}, \tag{A29b}$$

where

$$L_{r,n} = \Delta u_{r,n} - \frac{u_{r,n}}{r^2} - \frac{2}{r^2}\frac{\partial u_{\theta,n}}{\partial \theta} - Re\frac{\partial u_{r,n}}{\partial t}, \tag{A30a}$$

$$L_{\theta,n} = \Delta u_{\theta,n} - \frac{u_{\theta,n}}{r^2} + \frac{2}{r^2}\frac{\partial u_{r,n}}{\partial \theta} - Re\frac{\partial u_{\theta,n}}{\partial t}, \tag{A30b}$$

$$NL_{r,i,j} = u_{r,i}\frac{\partial u_{r,j}}{\partial r} + \frac{u_{\theta,i}}{r}\frac{\partial u_{r,j}}{\partial \theta} - \frac{u_{\theta,i}u_{\theta,j}}{r}, \tag{A30c}$$

$$NL_{\theta,i,j} = u_{r,i}\frac{\partial u_{\theta,j}}{\partial r} + \frac{u_{\theta,i}}{r}\frac{\partial u_{\theta,j}}{\partial \theta} + \frac{u_{r,i}u_{\theta,j}}{r}. \tag{A30d}$$

The structure of the expansion of the pressure is given by the next lemma.

LEMMA A.2. *For $n \in \mathbb{N}$, the pressure from (A28) has the form*

$$p_n = \begin{cases} \sum_{l=0}^{n/2} G_{2l}^n(r,t)\cos(2l\theta) & \text{for } n \text{ even}, \\ \sum_{l=0}^{(n-1)/2} G_{2l+1}^n(r,t)\cos((2l+1)\theta) & \text{for } n \text{ odd}. \end{cases} \tag{A31}$$

Proof. We will examine the case when n is odd, as showing the case when n is even entails the same procedure. To prove the result, we show that the r-component of (A28)

https://doi.org/10.1017/jfm.2026.11734 Published online by Cambridge University Press

can be expressed as a linear combination of $\{\cos(\theta), \cos(3\theta), \ldots, \cos(n\theta)\}$, and the θ-component can be expressed as a linear combination of $\{\sin(\theta), \sin(3\theta), \ldots, \sin(n\theta)\}$. We show this is true first for the linear terms, and then for the nonlinear terms.

We begin with the linear terms. From Lemma A.1, the stream function ψ_n has the form

$$\psi_n = \sum_{l=1}^{(n-1)/2} F^n_{2l+1}(r, t) \sin((2l+1)\theta). \tag{A32}$$

Substituting ψ_n into $L_{r,n}$, we obtain

$$L_{r,n} = \sum_{l=1}^{(n-1)/2} M^n_{2l+1}(r, t) \cos((2l+1)\theta), \tag{A33}$$

where

$$M^n_m(r, t) = -\frac{4m}{r^3}\left(-\frac{r^2}{4}\frac{\partial^2 F^n_m}{\partial r^2} - \frac{r}{4}\frac{\partial F^n_m}{\partial r} + \frac{m^2}{4}F^n_m + \frac{Re\, r^2}{4}\frac{\partial F^n_m}{\partial t}\right). \tag{A34}$$

Similarly,

$$L_{\theta,n} = \sum_{l=1}^{(n-1)/2} S^n_{2l+1}(r, t) \sin((2l+1)\theta), \tag{A35}$$

where

$$S^n_s(r, t) = -\frac{\partial^3}{\partial r^3}F^n_s - \frac{1}{r}\frac{\partial^2 F^n_s}{\partial r^2} + \left(\frac{s}{r}\right)^2\frac{\partial F^n_s}{\partial r} + \frac{1}{r^2}\frac{\partial F^n_s}{\partial r} - \frac{2s^2}{r^3}F^n_s + Re\,\frac{\partial^2 F^n_s}{\partial t\,\partial r}. \tag{A36}$$

We next examine the nonlinear terms $NL_{r,i,j}$ and $NL_{\theta,i,j}$ for $i + j = n$. Because n is odd, one of i or j is even, and the other is odd. Without loss of generality, choose i even and j odd. Using Lemma A.1 for the form of the stream function, we substitute the velocity into (A30*c*) for $NL_{r,i,j}$ to obtain

$$NL_{r,i,j} = \sum_{s=1}^{i/2}\sum_{q=0}^{(j-1)/2} A_{i,j}(r, t)\sin(2s\theta)\sin((2q+1)\theta) + B_{i,j}(r, t)\cos(2s\theta)\cos((2q+1)\theta), \tag{A37}$$

where

$$A_{i,j}(r, t) = -\frac{1}{r}\frac{\partial}{\partial r}F^i_{2s}(r, t)\frac{\partial}{\partial r}F^j_{2q+1}(r, t) + \frac{(2q+1)^2}{r^2}\frac{\partial}{\partial r}F^i_{2s}(r, t)\, F^j_{2q+1}(r, t) \tag{A38}$$

and

$$B_{i,j}(r, t) = \frac{2s}{r^3}(2q+1)\, F^i_{2s}(r, t)\left(r\frac{\partial}{\partial r}F^j_{2q+1}(r, t) - F^j_{2q+1}(r, t)\right). \tag{A39}$$

For (A37), we invoke the following trigonometric identities for $a, b \in \mathbb{N}$:

$$2\sin(a\theta)\sin(b\theta) = \cos((a-b)\theta) - \cos((a+b)\theta), \tag{A40a}$$

$$2\cos(a\theta)\cos(b\theta) = \cos((a-b)\theta) + \cos((a+b)\theta). \tag{A40b}$$

Because $1 \le s \le i/2$ and $1 \le q \le (j-1)/2$,

$$3 \le |2q + 2s + 1| \le i + j = n, \quad 1 \le |2q - 2s + 1| \le \max\{|i-3|, |j-2|\}, \tag{A41}$$

https://doi.org/10.1017/jfm.2026.11734 Published online by Cambridge University Press

and (A37) is equivalent to

$$NL_{r,i,j} = \sum_{l=0}^{(n-1)/2} J^n_{2l+1}(r,t)\cos((2l+1)\theta), \tag{A42}$$

for some functions $J^n_{2l+1}(r,t)$.

Similarly, we substitute the velocity into $NL_{\theta,i,j}$ of (A30*d*) to obtain

$$NL_{\theta,i,j} = \sum_{s=1}^{i/2}\sum_{q=0}^{(j-1)/2} E_{i,j}(r,t)\sin((2q+1)\theta)\cos(2s\theta) + F_{i,j}(r,t)\sin(2s\theta)\cos((2q+1)\theta), \tag{A43}$$

where

$$E_{i,j}(r,t) = -\frac{2s}{r}F^i_{2s}(r,t)\,\frac{\partial^2}{\partial r^2}F^j_{2q+1}(r,t) - \frac{2s}{r^2}F^i_{2s}(r,t)\,\frac{\partial}{\partial r}F^j_{2q+1}(r,t) \tag{A44}$$

and

$$F_{i,j}(r,t) = \frac{2q+1}{r}\,\frac{\partial}{\partial r}F^i_{2s}(r,t)\,\frac{\partial}{\partial r}F^j_{2q+1}(r,t). \tag{A45}$$

We simplify (A43) using the trigonometric identity from (A19) to obtain

$$NL_{\theta,i,j} = \sum_{l=0}^{(n-1)/2} K^n_{2l+1}(r,t)\sin((2l+1)\theta) \tag{A46}$$

for some functions $K^n_{2l+1}(r,t)$.

Finally, from (A33) and (A42), $\partial p_n/\partial r$ is composed of cosine functions with odd arguments, and similarly, from (A35) and (A46), $\partial p_n/\partial\theta$ is composed of sine functions with odd arguments. Integrating with respect to both r and θ, the solution structure of p_n is

$$p_n = \sum_{l=0}^{(n-1)/2} G^n_{2l+1}(r,t)\cos((2l+1)\theta). \tag{A47}$$

Therefore, (A31) has been proven. □

Appendix B. Establishing necessary conditions for pumping

In § 4.4, we showed that for frequency ratio $\alpha = 2$, the third-order terms proportional to $\sin(\theta)$ in the steady stream function (and $\cos(\theta)$ in the steady pressure) produce a net force. To extend the argument from § 4.4 to general frequency ratios, we derive necessary conditions for the presence of a steady term proportional to $\sin(\theta)$ in the stream function, or proportional to $\cos(\theta)$ in the pressure. Lemmas A.1 and A.2 state that $\sin(\theta)$ and $\cos(\theta)$ terms can only appear when n is odd. Therefore, the necessary condition for pumping is equivalent to finding order n so that n is odd, and ψ_n has a steady term.

B.1. *Frequencies at each order*

We first show which frequencies occur at each order. Suppose that the cylinder oscillates in the horizontal direction with the motion:

$$X(t) = \frac{\epsilon}{2}(\sin(at) + \sin(bt)), \tag{B1}$$

https://doi.org/10.1017/jfm.2026.11734 Published online by Cambridge University Press

where $a, b, \in \mathbb{Z}$ and $\gcd(a, b) = 1$. Examining the first-order solution (5.10), ψ_1 involves the terms proportional to $e^{\pm iat}$ and $e^{\pm ibt}$. To solve for the second-order solution (5.11), we substitute ψ_1 into the right-hand side of (5.6). From the products of the exponential functions, the frequencies arising at second order are all sums of $\pm a$ and $\pm b$. Generally, the solution structure of ψ_n will be determined by the products of exponentials from lower-order solutions. If ψ_n contains a term proportional to e^{ift}, then e^{ift} is related to $e^{\pm iat}$ and $e^{\pm ibt}$ by

$$e^{ift} = \left(e^{iat}\right)^{\xi_1} \left(e^{-iat}\right)^{\xi_2} \left(e^{ibt}\right)^{\xi_3} \left(e^{-ibt}\right)^{\xi_4} \tag{B2}$$

and

$$\xi_1 + \xi_2 + \xi_3 + \xi_4 = n, \quad \xi_i \geq 0, \ i = 1, 2, 3, 4. \tag{B3}$$

Therefore,

$$f = \xi^{(1)} a + \xi^{(2)} b, \tag{B4}$$

where

$$\xi^{(1)} = (\xi_1 - \xi_2), \tag{B5}$$

$$\xi^{(2)} = (\xi_3 - \xi_4). \tag{B6}$$

The above analysis is based on the structure of (5.6) for the stream function. We next consider the pressure, and show that the pressure at nth order involves the same frequencies as the stream function. To begin, we take the divergence of the Navier–Stokes equation, and use the divergence-free condition to obtain

$$\Delta p = -Re \, \nabla \cdot (\boldsymbol{u} \cdot \nabla \boldsymbol{u}). \tag{B7}$$

After expanding the solution in powers of ϵ, the pressure at nth order satisfies

$$\Delta p_n = -Re \sum_{i+j=n} \nabla \cdot \left(\boldsymbol{u}_i \cdot \nabla \boldsymbol{u}_j\right). \tag{B8}$$

The right-hand side of this equation involves the same quadratic nonlinearity of the velocity that appears on the right-hand side of (5.6) for the stream function. Thus the stream function and the pressure involve the same frequencies at each order.

B.2. *Existence of pumping*

We return to (B3)–(B6), which give the frequencies that occur at each order. A steady solution ($f = 0$) occurs when

$$0 = \xi^{(1)} a + \xi^{(2)} b. \tag{B9}$$

Solving this equation for $\xi^{(1)}$, we obtain

$$\xi^{(1)} = -\frac{b\xi^{(2)}}{a}. \tag{B10}$$

Because $\gcd(a, b) = 1$, and $\xi^{(1)}$ and $\xi^{(2)}$ are integers, solutions to this equation can be expressed as

$$\xi^{(1)} = \xi_1 - \xi_2 = cb, \quad \xi^{(2)} = \xi_3 - \xi_4 = -ca, \quad c \in \mathbb{Z}. \tag{B11}$$

Using these equations to eliminate ξ_1 and ξ_2 from (B3) gives the order at which steady solutions occur as

$$n = 2\,(\xi_2 + \xi_3) + c(a + b). \tag{B12}$$

https://doi.org/10.1017/jfm.2026.11734 Published online by Cambridge University Press

We use this last equation to prove Results 5.2 and 5.3.

B.2.1. *Proof of Result 5.2*
Let a and b be both odd. From (B12), because $a+b$ is even, steady terms can only occur at even orders. From Result 5.1, there is no pumping.

B.2.2. *Proof of Result 5.3*
Without loss of generality, choose a odd and b even. From (B12), steady terms occur at odd order n for c odd. The smallest odd order n is obtained by choosing $c=1$ and $\xi_2=\xi_3=0$, which is order $n=a+b$.

Appendix C. Numerical methods

C.1. *Immersed boundary method*

We use the immersed boundary method to solve the Navier–Stokes equations. The immersed boundary method uses an Eulerian coordinate system for the fluid, and a Lagrangian coordinate system for the immersed structures (i.e. cylinder or channel walls) (Peskin 2002). Let s be the parametric coordinate of a structure, and let $\boldsymbol{X}(s,t)$ be its position. We use capital letters $\boldsymbol{X}(s,t)$, $\boldsymbol{U}(s,t)$ and $\boldsymbol{F}(s,t)$ to define position, velocity and force density in Lagrangian coordinates, and similarly we use lowercase $p(\boldsymbol{x},t)$, $\boldsymbol{u}(\boldsymbol{x},t)$ and $\boldsymbol{f}(\boldsymbol{x},t)$ for pressure, velocity and force density in Eulerian coordinates.

The forces on the structures are applied to the surrounding fluid, and the fluid and structure move with the same velocity on the structure. The structural force density $\boldsymbol{F}(s,t)$ in Eulerian coordinates is given by

$$\boldsymbol{f}(\boldsymbol{x},t)=S\boldsymbol{F}=\int_{structure}\boldsymbol{F}(s,t)\,\delta(\boldsymbol{x}-\boldsymbol{X}(s,t))\,\mathrm{d}s, \tag{C1}$$

where $\delta(\boldsymbol{x})$ is the Dirac delta function. The operator S 'spreads' the the force density from the immersed structure to the surrounding fluid. Similarly, the fluid velocity is interpolated to the immersed structure by the adjoint of the spreading operator:

$$\boldsymbol{U}(s,t)=S^{*}\boldsymbol{u}=\int_{fluid}\boldsymbol{u}(\boldsymbol{x},t)\,\delta(\boldsymbol{x}-\boldsymbol{X}(s,t))\,\mathrm{d}\boldsymbol{x}. \tag{C2}$$

In our simulations, the motion of the structure is prescribed, and the force density on the structure, $\boldsymbol{F}(s,t)$, is determined implicitly by requiring that the fluid velocity match the prescribed velocity of the boundary:

$$S^{*}\boldsymbol{u}=\boldsymbol{U}_b. \tag{C3}$$

The full system describing the fluid and immersed boundaries is

$$\rho\left(\frac{\partial\boldsymbol{u}}{\partial t}+\boldsymbol{u}\cdot\nabla\boldsymbol{u}\right)=-\nabla p+\mu\,\Delta\boldsymbol{u}+S\boldsymbol{F}, \tag{C4}$$

$$\nabla\cdot\boldsymbol{u}=0, \tag{C5}$$

$$S^{*}\boldsymbol{u}=\boldsymbol{U}_b, \tag{C6}$$

where ρ is the fluid density, and μ is the fluid viscosity.

C.2. *Discretisation*

We solve on a doubly periodic domain discretised into points equally spaced by Δx, and structures are discretised by points equally spaced by $\Delta s\approx\Delta x$. We approximate

https://doi.org/10.1017/jfm.2026.11734 Published online by Cambridge University Press

the differential operators using Fourier pseudo-spectral methods. The discrete delta function is

$$\delta = \delta_{\Delta x}(x)\,\delta_{\Delta x}(y), \tag{C7}$$

where

$$\delta_{\Delta x}(x) = \begin{cases} \dfrac{1}{4\,\Delta x}\left(1+\cos\left(\dfrac{\pi x}{2\,\Delta x}\right)\right) & \text{if } |x| < 2\,\Delta x, \\ 0 & \text{otherwise.} \end{cases} \tag{C8}$$

The discretised spread (C1) and interpolating (C2) operators are

$$f_{i,j} = S\boldsymbol{F} = \Delta s \sum_k F_k\,\delta_{\Delta x}\,(x_i - X_k)\;\delta_{\Delta x}\left(y_j - Y_k\right), \tag{C9}$$

$$U_k = S^*\boldsymbol{u} = \Delta x^2 \sum_{i,j} u_{i,j}\,\delta_{\Delta x}\,(x_i - X_k)\;\delta_{\Delta x}(y_j - Y_k). \tag{C10}$$

For the temporal discretisation, we use a second-order IMEX scheme, named SBDF in Ascher, Ruuth & Wetton (1995), in which the nonlinear terms are treated explicitly in time, and the terms for the viscous force and structure force are treated implicitly in time with BDF2. The discretised system is

$$\rho\left(\frac{3\boldsymbol{u}^{n+1} - 4\boldsymbol{u}^n + \boldsymbol{u}^{n-1}}{2\,\Delta t} + 2\boldsymbol{u}^n \cdot G\boldsymbol{u}^n - \boldsymbol{u}^{n-1}\cdot G\boldsymbol{u}^{n-1}\right) = -Gp^{n+1} + \mu L\boldsymbol{u}^{n+1} + S\boldsymbol{F}^{n+1}, \tag{C11}$$

$$D\boldsymbol{u}^{n+1} = 0, \tag{C12}$$

$$S^*\boldsymbol{u}^{n+1} = \boldsymbol{U}_b^{n+1}, \tag{C13}$$

where G, D, L represent the discrete gradient, divergence and Laplacian, respectively. Because the nonlinear terms are treated explicitly in time, the resulting system to solve at each time step is linear. In block form, the system is

$$\begin{bmatrix} A & G & -S \\ D & 0 & 0 \\ S^* & 0 & 0 \end{bmatrix} \begin{bmatrix} \boldsymbol{u} \\ p \\ \boldsymbol{F} \end{bmatrix}^{n+1} = \begin{bmatrix} \boldsymbol{g} \\ 0 \\ \boldsymbol{U}_b^{n+1} \end{bmatrix}, \tag{C14}$$

where

$$A = \frac{3\rho}{2\,\Delta t} I - \mu L, \tag{C15}$$

and the known terms are

$$g = \rho\left(-2\boldsymbol{u}^n \cdot G\boldsymbol{u}^n + \boldsymbol{u}^{n-1}\cdot G\boldsymbol{u}^{n-1} - \frac{-4\boldsymbol{u}^n + \boldsymbol{u}^{n-1}}{2\,\Delta t}\right). \tag{C16}$$

We solve (C14) at each time step by first solving for the force density that satisfies

$$S^*\mathcal{L}^{-1}S\boldsymbol{F} = \boldsymbol{U}_b^{n+1} - S^*\mathcal{L}^{-1}\boldsymbol{g}, \tag{C17}$$

where we denote the operator that maps the fluid force density to the fluid velocity by $\mathcal{L}^{-1}$. Specifically, suppose that $\boldsymbol{u}$ and p satisfy the system

$$\begin{bmatrix} A & G \\ D & 0 \end{bmatrix} \begin{bmatrix} \boldsymbol{u} \\ p \end{bmatrix} + \begin{bmatrix} f \\ 0 \end{bmatrix} = 0. \tag{C18}$$

https://doi.org/10.1017/jfm.2026.11734 Published online by Cambridge University Press

Δx	Δt	Flux	Difference	Ratio	$\log_2$(Ratio)
8/256	1.00×10^{-2}	9.6044×10^{-2}	—	—	—
8/512	5.00×10^{-3}	1.0130×10^{-1}	5.2573×10^{-3}	—	—
8/1024	2.50×10^{-3}	1.0279×10^{-1}	1.4937×10^{-3}	3.5197	1.8155
8/2048	1.25×10^{-3}	1.0324×10^{-1}	4.4149×10^{-4}	3.3833	1.7584

Table 1. Refinement study for the flux with simultaneous refinement of space and time for the flow around an oscillating cylinder in a square 8×8 domain with periodic boundary conditions at $Re = 10$, amplitude $\epsilon = 0.5$, and time $T = 100$.

Δt	Flux	Difference	Ratio	$\log_2$(Ratio)
1.000×10^{-2}	9.6044×10^{-2}	—	—	—
5.000×10^{-3}	1.0086×10^{-1}	4.8185×10^{-3}	—	—
2.500×10^{-3}	1.0175×10^{-1}	8.8700×10^{-4}	5.4324	2.4416
1.250×10^{-3}	1.0191×10^{-1}	1.6291×10^{-4}	5.4447	2.4448
6.250×10^{-4}	1.0194×10^{-1}	3.2425×10^{-5}	5.0243	2.3289
3.125×10^{-4}	1.0195×10^{-1}	7.1196×10^{-6}	4.5543	2.1872

Table 2. Refinement study in time only for the flux with the space step fixed at $\Delta x = 8/256$ for the flow around an oscillating cylinder in a square 8×8 domain with periodic boundary conditions at $Re = 10$, amplitude $\epsilon = 0.5$, and time $T = 100$.

Then $\mathcal{L}^{-1}$ is

$$\boldsymbol{u} = \mathcal{L}^{-1} \boldsymbol{f}. \tag{C19}$$

The operator $\mathcal{L}^{-1}$ can be applied efficiently using the fast Fourier transform. We solve (C17) with a Krylov method, which requires a preconditioner for efficiency. For preconditioning, we explicitly form the dense matrix representing $S^* \mathcal{L}^{-1} S$ at time 0, and compute its Cholesky factorisation. This work is performed before running the simulation.

The grid resolution for channel simulations was $\Delta x = 8/256$, so that there were 256 grid points in the vertical direction, or equivalently 64 points along the cylinder diameter. The time step was $\Delta t = 5.00 \times 10^{-4}$. The tolerance for the conjugate gradient method used to solve (C17) was 1×10^{-3}.

For the simulations presented in figure 1, the grid resolution was $\Delta x = 8/512$ and the time step was $\Delta t = 5.00 \times 10^{-3}$. Table 1 shows the results of a mesh refinement study on this problem which shows that the time-averaged flux converges at approximately second order. Using the finest mesh ($\Delta x = 8/2048$, $\Delta t = 1.25 \times 10^{-3}$) as the solution, we estimate that the error in the flux for $\Delta x = 8/512$ and $\Delta t = 5.00 \times 10^{-3}$ is approximately 1.9 %.

In the channel simulations, we used a coarser spatial resolution $\Delta x = 8/256$, but a smaller time step $\Delta t = 5.00 \times 10^{-4}$. Fixing the grid resolution as $\Delta x = 8/256$ and refining the time step, we find that the flux converges at approximately second order in Δt (table 2). For the smallest time step, the relative changes in flux are on the scale of 10^{-4}, and thus, the spatial error is dominant. Comparing with the fluxes from the space-time refinement study in table 1, we estimate the error in our numerical simulations to be on the scale 1–2 %.

https://doi.org/10.1017/jfm.2026.11734 Published online by Cambridge University Press

References

Agarwal, S., Rallabandi, B. & Hilgenfeldt, S. 2018 Inertial forces for particle manipulation near oscillating interfaces. *Phys. Rev. Fluids* **3** (10), 104201.

Ahmed, D., Mao, X., Juluri, B.K. & Huang, T.J. 2009 A fast microfluidic mixer based on acoustically driven sidewall-trapped microbubbles. *Microfluid Nanofluid* **7**, 727–731.

Ahmed, S., Wang, W., Bai, L., Gentekos, D.T., Hoyos, M. & Mallouk, T.E. 2016 Density and shape effects in the acoustic propulsion of bimetallic nanorod motors. *ACS Nano* **10** (4), 4763–4769.

Andrade, E.N.D.C. 1931 On the circulations caused by the vibration of air in a tube. *Proc. R. Soc. Lond. A* **134** (824), 445–470.

Ascher, U.M., Ruuth, S.J. & Wetton, B.T.R. 1995 Implicit–explicit methods for time-dependent partial differential equations. *SIAM J. Numer. Anal.* **32** (3), 797–823.

Batchelor, G.K. 2000 *An Introduction to Fluid Dynamics*. Cambridge University Press.

Bertelsen, A., Svardal, A. & Tjøtta, S. 1973 Nonlinear streaming effects associated with oscillating cylinders. *J. Fluid Mech.* **59** (3), 493–511.

Carrière, Z. 1929 Analyse ultramicroscopique des vibrations aériennes. *J. Phys. Radium* **10** (5), 198–208.

Chong, K., Kelly, S.D., Smith, S. & Eldredge, J.D. 2013 Inertial particle trapping in viscous streaming. *Phys. Fluids* **25** (3), 033602.

Collis, J.F., Chakraborty, D. & Sader, J.E. 2017 Autonomous propulsion of nanorods trapped in an acoustic field. *J. Fluid Mech.* **825**, 29–48.

Davidson, B.J. & Riley, N. 1972 Jets induced by oscillatory motion. *J. Fluid Mech.* **53** (2), 287–303.

Hashemi, A., Gilman, E.T. & Khair, A.S. 2024 A multiple-timing analysis of temporal ratcheting. *Eur. Phys. J. E* **47** (4), 1–8.

Hashemi, A., Tahernia, M., Hui, T.C., Ristenpart, W.D. & Miller, G.H. 2022 Net motion induced by nonantiperiodic vibratory or electrophoretic excitations with zero time average. *Phys. Rev. E* **105** (6), 065001.

Holtsmark, J., Johnsen, I., Sikkeland, T. & Skavlem, S. 1954 Boundary layer flow near a cylindrical obstacle in an oscillating, incompressible fluid. *J. Acoust. Soc. Am.* **26** (1), 26–39.

Huang, P.-H., Nama, N., Mao, Z., Li, P., Rufo, J., Chen, Y., Xie, Y., Wei, C.-H., Wang, L. & Huang, T.J. 2014 A reliable and programmable acoustofluidic pump powered by oscillating sharp-edge structures. *Lab on a Chip* **14** (22), 4319–4323.

Huang, P.-H., Xie, Y., Ahmed, D., Rufo, J., Nama, N., Chen, Y., Chan, C.Y. & Huang, T.J. 2013 An acoustofluidic micromixer based on oscillating sidewall sharp-edges. *Lab on a Chip* **13** (19), 3847–3852.

Hui, T.C., Zhang, X., Adiga, D., Miller, G.H. & Ristenpart, W.D. 2024 Vibrational manipulation of dry granular materials in lab-on-a-chip devices. *Lab on a Chip* **24** (4), 966–974.

Kotas, C.W., Yoda, M. & Rogers, P.H. 2008 Steady streaming flows near spheroids oscillated at multiple frequencies. *Exp. Fluids* **45**, 295–307.

Kumar, H., Tawhai, M.H., Hoffman, E.A. & Lin, C.-L. 2011 Steady streaming: a key mixing mechanism in low-Reynolds-number acinar flows. *Phys. Fluids* **23** (4), 041902.

Li, P., Nunn, A.R., Brumley, D.R., Sader, J.E. & Collis, J.F. 2024 The propulsion direction of nanoparticles trapped in an acoustic field. *J. Fluid Mech.* **984**, R1.

Lippera, K., Dauchot, O., Michelin, S. & Benzaquen, M. 2019 No net motion for oscillating near-spheres at low Reynolds numbers. *J. Fluid Mech.* **866**, R1.

Liu, R.H., Lenigk, R. & Grodzinski, P. 2003 Acoustic micromixer for enhancement of DNA biochip systems. *J. Micro/Nanolithography MEMS MOEMS* **2** (3), 178–184.

Lutz, B.R., Chen, J. & Schwartz, D.T. 2005 Microscopic steady streaming eddies created around short cylinders in a channel: flow visualization and Stokes layer scaling. *Phys. Fluids* **17** (2), 023601.

Marmottant, P. & Hilgenfeldt, S. 2004 A bubble-driven microfluidic transport element for bioengineering. *Proc. Natl Acad. Sci. USA* **101** (26), 9523–9527.

Marmottant, P., Raven, J.P., Gardeniers, H., Bomer, J.G. & Hilgenfeldt, S. 2006 Microfluidics with ultrasound-driven bubbles. *J. Fluid Mech.* **568**, 109–118.

Mutlu, B.R., Edd, J.F. & Toner, M. 2018 Oscillatory inertial focusing in infinite microchannels. *Proc. Natl Acad. Sci. USA* **115** (30), 7682–7687.

Nadal, F. & Lauga, E. 2014 Asymmetric steady streaming as a mechanism for acoustic propulsion of rigid bodies. *Phys. Fluids* **26** (8), 082001.

Nadal, F. & Michelin, S. 2020 Acoustic propulsion of a small, bottom-heavy sphere. *J. Fluid Mech.* **898**, A10.

Patel, M.V., Nanayakkara, I.A., Simon, M.G. & Lee, A.P. 2014 Cavity-induced microstreaming for simultaneous on-chip pumping and size-based separation of cells and particles. *Lab on a Chip* **14** (19), 3860–3872.

https://doi.org/10.1017/jfm.2026.11734 Published online by Cambridge University Press

PESKIN, C.S. 2002 The immersed boundary method. *Acta Numerica* **11**, 479–517.
RALLABANDI, B., WANG, C. & HILGENFELDT, S. 2014 Two-dimensional streaming flows driven by sessile semicylindrical microbubbles. *J. Fluid Mech.* **739**, 57–71.
RANEY, W.P., CORELLI, J.C. & WESTERVELT, P.J. 1954 Acoustical streaming in the vicinity of a cylinder. *J. Acoust. Soc. Am.* **26** (6), 1006–1014.
REZNIK, D. & CANNY, J. 1998 The coulomb pump: a novel parts feeding method using a horizontally-vibrating surface. In *Proceedings. 1998 IEEE International Conference on Robotics and Automation* (Cat. No. 98CH36146), vol. 1, pp. 869–874. IEEE.
REZNIK, D., CANNY, J. & GOLDBERG, K. 1997 Analysis of part motion on a longitudinally vibrating plate. In *Proceedings of the 1997 IEEE/RSJ International Conference on Intelligent Robot and Systems. Innovative Robotics for Real-World Applications. IROS'97*, vol. 1, pp. 421–427. IEEE.
REZNIK, D.S. & CANNY, J.F. 2001 C'mon part, do the local motion!. In *Proceedings 2001 ICRA. IEEE International Conference on Robotics and Automation (Cat. No. 01CH37164)*, vol. 3, pp. 2235–2242. IEEE.
RILEY, N. 1965 Oscillating viscous flows. *Mathematika* **12** (2), 161–175.
RILEY, N. 2001 Steady streaming. *Annu. Rev. Fluid Mech.* **33** (1), 43–65.
SABRINA, S., TASINKEVYCH, M., AHMED, S., BROOKS, A.M., OLVERA DE LA CRUZ, M., MALLOUK, T.E. & BISHOP, K.J.M. 2018 Shape-directed microspinners powered by ultrasound. *ACS Nano* **12** (3), 2939–2947.
SCHLICHTING, H. 1932 Berechnung ebener periodischer grenzschichtstromungen. *Phys. Z.* **33**, 327–335.
STUART, J.T. 1966 Double boundary layers in oscillatory viscous flow. *J. Fluid Mech.* **24** (4), 673–687.
SUMNER, L., MESTEL, J. & REICHENBACH, T. 2021 Steady streaming as a method for drug delivery to the inner ear. *Sci. Rep. UK* **11** (1), 57.
THAMEEM, R., RALLABANDI, B. & HILGENFELDT, S. 2016 Particle migration and sorting in microbubble streaming flows. *Biomicrofluidics* **10** (1), 014124.
TOVAR, A.R. & LEE, A.P. 2009 Lateral cavity acoustic transducer. *Lab on a Chip* **9** (1), 41–43.
TOVAR, A.R., PATEL, M.V. & LEE, A.P. 2011 Lateral air cavities for microfluidic pumping with the use of acoustic energy. *Microfluid Nanofluid* **10**, 1269–1278.
VOLK, A., ROSSI, M., RALLABANDI, B., KÄHLER, C.J., HILGENFELDT, S. & MARIN, A. 2020 Size-dependent particle migration and trapping in three-dimensional microbubble streaming flows. *Phys. Rev. Fluids* **5** (11), 114201.
WANG, C., JALIKOP, S.V. & HILGENFELDT, S. 2012*a* Efficient manipulation of microparticles in bubble streaming flows. *Biomicrofluidics* **6** (1), 012801.
WANG, C., RALLABANDI, B. & HILGENFELDT, S. 2013 Frequency dependence and frequency control of microbubble streaming flows. *Phys. Fluids* **25** (2), 022002.
WANG, C.-Y. 1968 On high-frequency oscillatory viscous flows. *J. Fluid Mech.* **32** (1), 55–68.
WANG, W., CASTRO, L.A., HOYOS, M. & MALLOUK, T.E. 2012*b* Autonomous motion of metallic microrods propelled by ultrasound. *ACS Nano* **6** (7), 6122–6132.
WATSON, G.N. 1922 *A Treatise on the Theory of Bessel Functions*. Cambridge University Press.
WILLIS, N. & HOHENEGGER, C. 2024 Quasi-three-dimensional viscous steady streaming in a rectangular channel past a cylinder. *SIAM J. Appl. Maths* **84** (5), 1957–1981.
ZHANG, X., HUI, T.C., RISTENPART, W.D. & MILLER, G.H. 2024*a* Theoretical velocity of an object frictionally coupled to a two-mode vibrating plate. *Phys. Rev. E* **110** (2), 024212.
ZHANG, X., MINTEN, J. & RALLABANDI, B. 2024*b* Particle hydrodynamics in acoustic fields: unifying acoustophoresis with streaming. *Phys. Rev. Fluids* **9** (4), 044303.
ZHANG, X. & RALLABANDI, B. 2024 Elasto-inertial rectification of oscillatory flow in an elastic tube. *J. Fluid Mech.* **996**, A16.

https://doi.org/10.1017/jfm.2026.11734 Published online by Cambridge University Press